JACS
JOURNAL OF THE AMERICAN CHEMICAL SOCIETY
Article
pubs.acs.org/JACS

Synthetic Control Over Photoinduced Electron Transfer in Phosphorescence Zinc Sensors

Hana Woo,[§,†] Somin Cho,[§,†] Yejee Han,[§] Weon-Sik Chae,[⊥] Dae-Ro Ahn,[∥] Youngmin You,*[,§,‡] and Wonwoo Nam*[,§]

[§]Department of Bioinspired Science, Ewha Womans University, Daehyun-dong, Seodaemun-gu, Seoul 120-750, Korea
[⊥]Korea Basic Science Institute, Gangneung Center, Gangneung, Gangwondo 210-702, Korea
[∥]Center for Theragnosis, Biomedical Research Institute, Korea Institute of Science and Technology, Seoul 130-650, Korea

Supporting Information

ABSTRACT: Despite the promising photofunctionalities, phosphorescent probes have been examined only to a limited extent, and the molecular features that provide convenient handles for controlling the phosphorescence response have yet to be identified. We synthesized a series of phosphorescence zinc sensors based on a cyclometalated heteroleptic Ir(III) complex. The sensor construct includes two anionic cyclometalating ligands and a neutral diimine ligand that tethers a di(2-picolyl)amine (DPA) zinc receptor. A series of cyclometalating ligands with a range of electron densities and band gap energies were used to create phosphorescence sensors. The sensor series was characterized by variable-temperature steady-state and transient photoluminescence spectroscopy studies, electrochemical measurements, and quantum chemical calculations based on time-dependent density functional theory. The studies demonstrated that the suppression of nonradiative photoinduced electron transfer (PeT) from DPA to the photoexcited Ir^{IV} species provided the underlying mechanism that governed the phosphorescent response to zinc ions. Importantly, the Coulombic barrier, which was located on either the cyclometalating ligand or the diimine ligand, negligibly influenced the PeT process. Phosphorescence modulation by PeT strictly obeyed the Rehm−Weller principle, and the process occurred in the Marcus-normal region. These findings provide important guidelines for improving sensing performance; an efficient phosphorescence sensor should include a cyclometalating ligand with a wide band gap energy and a deep oxidation potential. Finally, the actions of the sensor were demonstrated by visualizing the intracellular zinc ion distribution in HeLa cells using a confocal laser scanning microscope and a photoluminescence lifetime imaging microscope.

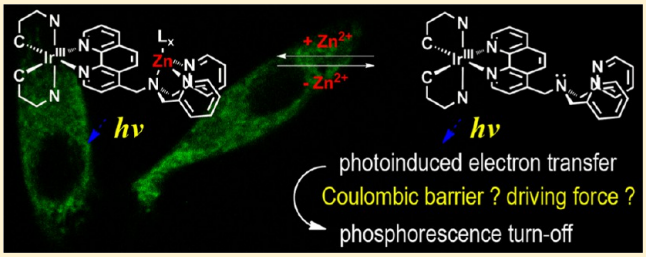

1. INTRODUCTION

Photoluminescent sensors are ideal for cellular studies because the instrumentation required for luminescence detection is relatively simple, a high spatiotemporal resolution may be obtained, the signal sensitivity is high, and the dynamic range (DR) is broad. The pioneering works by Tsien et al. demonstrated the utility of photoluminescence sensors for visualizing calcium ion distributions in the context of key cellular processes.[1,2] This initial success stimulated the development of a wide range of photoluminescence sensors for visualizing biological metal ion distributions,[3−5] such as labile zinc.[6−16] A variety of photophysical mechanisms, including intramolecular charge transfer,[17,18] twisted intramolecular charge transfer,[19] and excited-state intramolecular proton transfer,[20−24] have been employed in the design of fluorescence metal ion sensors. Among the photophysical strategies, photoinduced electron transfer (PeT) has been the most successful.[14,25−34]

PeT-based sensing relies on redox potential switching in a receptor site due to metal coordination.[35−37] In the absence of a metal ion, PeT occurs from the receptor to a photoexcited chromophore to transiently generate a nonemissive radical ion pair.[38] Subsequent back electron transfer rapidly restores the neutral form of the sensor. Metal ion coordination inhibits PeT by lowering the oxidation potential of the receptor. The switching process restores the photoluminescence of the chromophore. The net effect is a photoluminescence turn-on of the sensor. The DR of this sensing mechanism increases in proportion with the extent of PeT, where DR is defined as the ratio of the brightness of the photoluminescence-on state to the brightness of the photoluminescence-off state (brightness = absorbance at the photoexcitation wavelength × photoluminescence quantum yield).

Because structural modifications can alter the pK_a[39−45] and the metal ion binding strength[46−50] of the metal ion receptor, synthetic optimization efforts for the purpose of improving PeT have been directed mainly toward the chromophore.[51,52] One

Received: December 17, 2012
Published: March 4, 2013

   dx.doi.org/10.1021/ja3123202 | J. Am. Chem. Soc. 2013, 135, 4771−4787

Scheme 1. Synthesis and Structures of the Phosphorescence Zinc Sensors $[Ir(C\wedge N)_2(N\wedge N)]PF_6$

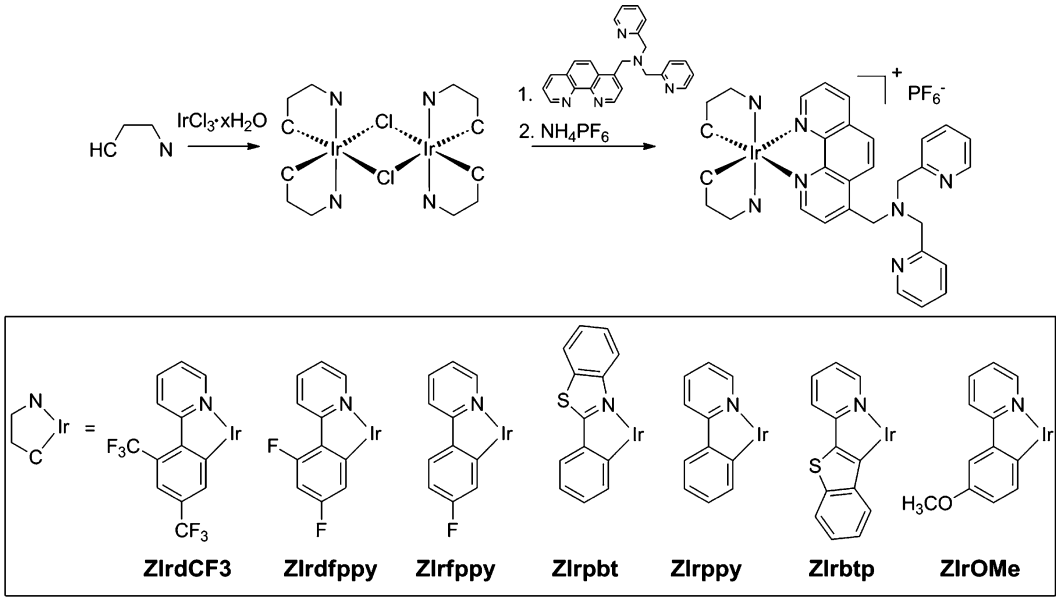

viable strategy involves stabilizing the excited-state reduction potential of the chromophore (E^*_{red}) because the driving force for PeT ($-\Delta G_{PeT}$) is linearly proportional to the potential difference between E^*_{red} and the ground-state oxidation potential of the receptor (E°_{ox}): $-\Delta G_{PeT} = -e[E^\circ_{ox}(\text{receptor}) - E^*_{red}(\text{chromophore})]$. A larger DR value may be obtained by lowering E^*_{red} of the chromophore. Synthetic control over E^*_{red}, which is determined according to the relationship $E^*_{red} = E^\circ_{red} + \Delta E_{00}$, may be achieved through strategies that tune the ground-state reduction potential (E°_{red}) and the photoexcited state energy (ΔE_{00}). Independent control over E°_{red} and ΔE_{00} is not straightforward, however, due to strong coupling between the electrochemical properties and the electronic state energy. Lowering E^*_{red} is even more difficult in near-infrared-fluorescent chromophores than visible-fluorescent ones due to the small ΔE_{00}.[53] These difficulties present significant challenges in the development of photoluminescence sensors based on the PeT mechanism.

A promising approach to conquering this challenge involves the use of long-lifetime emitters, such as phosphorescent transition metal complexes. Because the extent of photoluminescence modulation increases in proportion to the relative rates of PeT and the radiative transition process, greater DR values are expected for long-lifetime emitters.[54] Considering that the absorbance value is invariant under the metal coordination in most PeT-based sensors, the DR value can be expressed as eq 1,

$$\begin{aligned} \text{DR} &= \Phi/\Phi_0 = (k_r + k_{nr} + k_{PeT})/(k_r + k_{nr}) \\ &= 1 + k_{PeT}/(k_r + k_{nr}) \end{aligned} \quad (1)$$

where Φ and Φ_0 are photoluminescence quantum yields in the absence and presence of PeT, respectively, and k_r, k_{PeT}, and k_{nr} are the rate constants for the radiative transition, PeT, and other nonradiative transitions, respectively. Equation 1 implies that a chromophore with a longer photoluminescence lifetime (τ_{obs}) would display a larger DR value because $k_r = \Phi/\tau_{obs}$. Phosphorescent Ir(III) complexes yield $\tau_{obs} \approx 10^{-6}$ s, with Φ values comparable to those of typical fluorophores having $\tau_{obs} \approx 10^{-9}$–$10^{-7}$ s; therefore, the complexes can potentially provide a 10–1000-fold enhancement in the DR value relative to the values for fluorescence sensors. The use of long-lifetime emitters is additionally advantageous because time-gated luminescence detection methods can be employed to remove autofluorescence and scattered lights. Several research groups have demonstrated significant improvements in the signal-to-noise ratio upon implementation of time-gated discrimination in the detection of long-lifetime signals.[55−60]

We recently developed a phosphorescence zinc sensor based on a heteroleptic Ir(III) complex $[Ir(C\wedge N)_2(N\wedge N)]^+$ comprising 1,10-phenanthroline (N∧N) and two anionic cyclometalating (C∧N) ligands. The zinc sensor successfully indicated the presence of intracellular zinc ions through the changes in the phosphorescence intensity and the phosphorescence lifetime.[61] These phosphorescent signaling capabilities appear to be highly sensitive to the ligand structures because a similar Ir(III) complex with different substituents of C∧N ligands did not produce phosphorescence responses in aqueous milieu.[62] This discrepancy prompted us to investigate the molecular factors underlying the phosphorescence response in an effort to improve the phosphorescence DR. To this end, we systematically varied the C∧N ligand structures in the Ir(III) complexes (Scheme 1). We envisioned that this structural variation would allow us to address two important issues regarding PeT in phosphorescence signaling: (1) E^*_{red} engineering and (2) the influence of a Coulombic barrier.[63] The C∧N ligand structure variations were expected to alter the E°_{red} values of the corresponding Ir(III) complexes because the lowest unoccupied molecular orbital (LUMO) of a typical cyclometalated Ir(III) complex involves the π^* orbitals of their C∧N ligands.[64−70] Electron-withdrawing substituents, such as −F and $-CF_3$, were expected to lower E°_{red}, whereas electron-donating groups, such as $-OCH_3$, were expected to have the opposite effect. The diimine (N∧N) ligand (i.e., 1,10-phenanthroline) was left unmodified, allowing the PeT process to be interpreted solely on the basis of the C∧N ligand control.

In the $[Ir^{III}(C\wedge N)_2(N\wedge N)]^+$ construct, the global LUMO contributing to the lowest triplet transition can be localized either on the C∧N ligand or the N∧N ligand (Scheme 2).[61,71−76] For example, 2-(2,4-difluorophenyl)pyridinate

dx.doi.org/10.1021/ja3123202 | J. Am. Chem. Soc. 2013, 135, 4771−4787

Scheme 2. Schematic Representation of the Photoelectrochemical Processes in the Zinc-Free (Upper Part) and the Zinc-Bound (Lower Part) Phosphorescence Sensors[a]

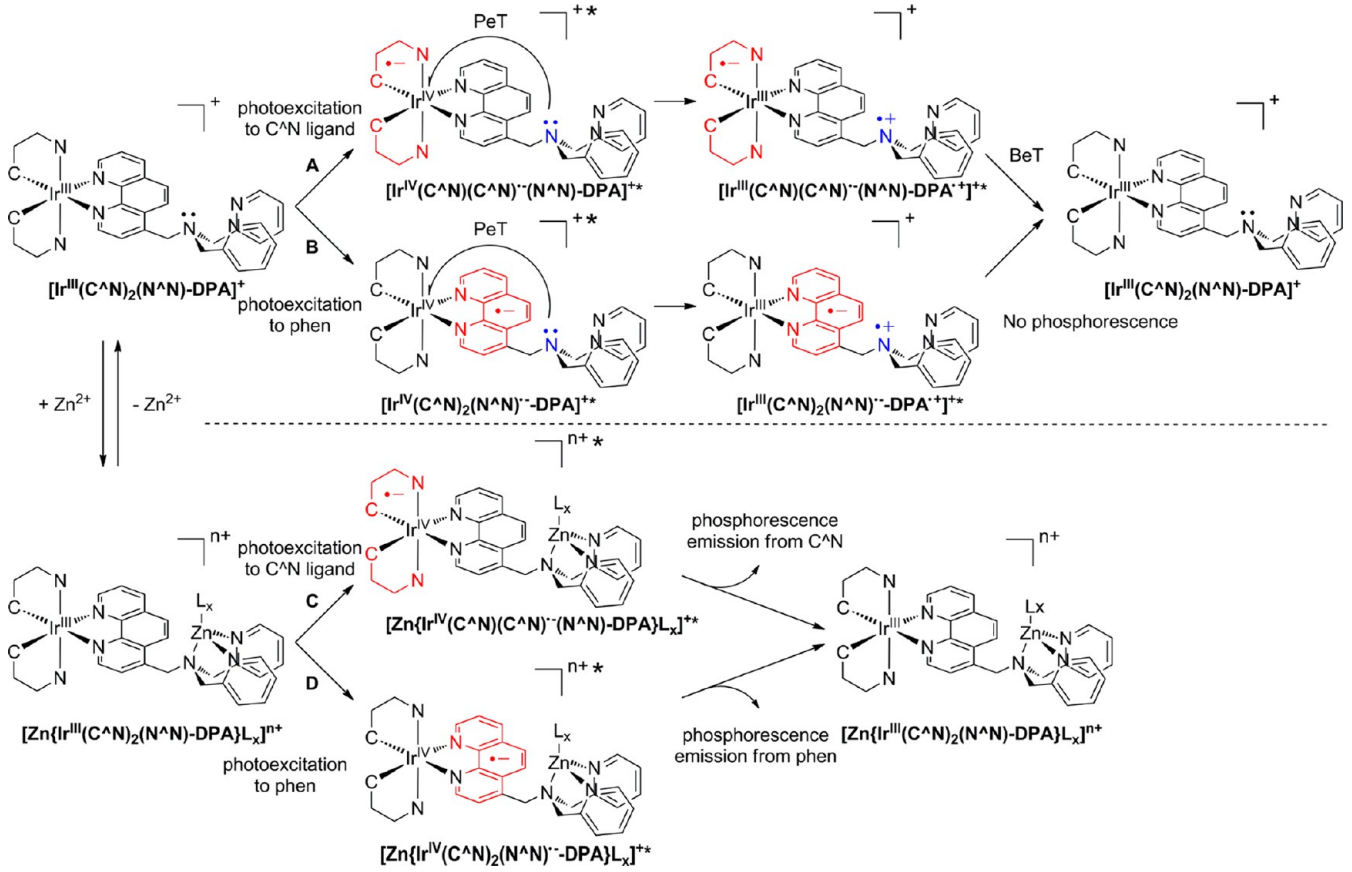

[a]Abbreviations: PeT, photoinduced electron transfer; BeT, back electron transfer. Routes A and C show photoexcitation to the C∧N ligand; routes B and D show photoexcitation to the 1,10-phenanthroline (phen) ligand.

(dfppy), which has a higher electronic energy than 1,10-phenanthroline, contributes weakly to the global LUMO, whereas 2-(2-benzo[*b*]thienyl)pyridinate (btp), with a lower electronic energy, dominates the global LUMO. Therefore, the triplet metal-to-ligand charge-transfer (^{3}MLCT) transition produces two different radical ion pairs, $[Ir^{IV}(C\wedge N)(C\wedge N)^{\bullet-}(N\wedge N)]^{+*}$ or $[Ir^{IV}(C\wedge N)_2(N\wedge N)^{\bullet-}]^{+*}$ formed via an electronic transition to either the C∧N ligand (routes A and C in Scheme 2) or the N∧N ligand (routes B and D in Scheme 2), respectively. In the latter case, the subsequent PeT process from the di(2-picolyl)amino (DPA) moiety to the Ir^{IV} center would encounter a higher degree of Coulombic repulsion due to the negative charge on the N∧N ligand (i.e., $(N\wedge N)^{\bullet-}$). The importance of the Coulombic barrier was suggested by Wenger et al. in a study of the photosensitization of long-range electron transfer.[63] The series of Ir(III) complexes described herein were designed to examine whether the Coulombic barrier would indeed retard PeT. The location of the Coulombic barrier in this series was tuned according to C∧N ligand. The C∧N ligand control additionally tuned the phosphorescence peak wavelengths,[77−79] thereby enriching the library of sensors for multichannel microscopy.[80]

Here, we report the use of synthetic control to tune the phosphorescence responses of a series of zinc sensors (ZIr series in Scheme 1). A series of C∧N ligands with different electronic structures, 2-(2,4-di(trifluoromethyl)phenyl)-pyridinate (dCF3), 2-(2,4-difluorophenyl)pyridinate (dfppy), 2-(4-fluorophenyl)pyridinate (fppy), 2-phenylbenzo[*d*]-thiazolate (pbt), 2-phenylpyridinate (ppy), 2-(2-benzo[*b*]-thienyl)pyridinate (btp), and 2-(3-methoxyphenyl)pyridinate (OMe), were incorporated into heteroleptic Ir(III) complexes to afford seven phosphorescence sensors. The phosphorescence responses were characterized, revealing a profound effect of the C∧N ligand. Steady-state and transient photoluminescence measurements, electrochemical characterization, and time-dependent density functional theory (TD-DFT) calculations were performed to establish the relationships between the DR value and several molecular parameters: E^*_{red}, $-\Delta G_{PeT}$, and k_r/k_{nr}. The dependences of the PeT rate constant (k_{PeT}) and $-\Delta G_{PeT}$ on these parameters were investigated. The position of the Coulombic barrier in each phosphorescence sensor was determined by analyzing the temperature-dependent phosphorescence spectrum and TD-DFT calculation results. Finally, the zinc detection capabilities of ZIrdCF3 were examined in aqueous buffered solutions at pH 7.4. The utility of the sensor was demonstrated by monitoring intracellular zinc ion in HeLa cells using confocal laser scanning microscopy and photoluminescence lifetime imaging microscopy techniques.

2. RESULTS AND DISCUSSION

Synthesis of the Phosphorescence Zinc Sensors. The synthetic routes to the seven phosphorescence zinc sensors are depicted in Scheme 1. The Pd(0)-catalyzed Suzuki−Miyaura cross-coupling between arylhalide and aryl boronic acid was

dx.doi.org/10.1021/ja3123202 | J. Am. Chem. Soc. 2013, 135, 4771−4787

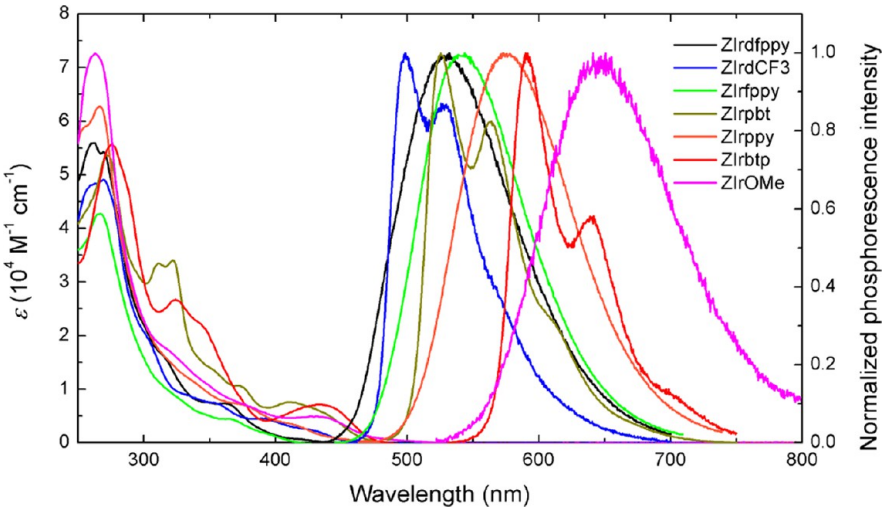

Figure 1. UV−vis absorption and normalized phosphorescence spectra of 10 μM zinc sensors (CH_3CN). Photoexcitation wavelengths: 359 (ZIrdfppy), 393 (ZIrdCF3), 362 (ZIrfppy), 377 (ZIrppy), 412 (ZIrpbt), 434 (ZIrbtp), and 377 nm (ZIrOMe).

Table 1. Photophysical Characterization for the Phosphorescence Sensors (ZIr Series) and Their Reference Compounds (Ir Series)[a]

compound	λ_{em} (nm)[b]	$\Delta\nu$ (cm^{-1})[c]	Φ (%)[d]	DR[e]	τ_{obs} (μs)[f]	k_r ($\times10^4$ s^{-1})[g]	k_{nr} ($\times10^5$ s^{-1})[h]
IrdCF3	499	1353	21 ± 1.5		5.13	4.09	1.54
ZIrdCF3	498	1394	1.4 ± 0.8	12	0.0000512[j]	27.3	193
ZIrdCF3 + Zn^{2+} [i]	498	1349	17 ± 2.3		5.35	3.18	1.55
Irdfppy	518	1418	12 ± 1.3		1.92	5.73	4.64
ZIrdfppy	525	1367	0.45 ± 0.17	31	0.0095[j]	47.4	1047
ZIrdfppy + Zn^{2+} [i]	540	n.d.	14 ± 2.0		1.71	8.19	5.03
Irpbt	525	1388	14 ± 1.2		4.82	2.90	1.78
ZIrpbt	526	1395	12 ± 0.72	0.91	3.78	3.17	2.32
ZIrpbt + Zn^{2+} [i]	575	1410	11 ± 1.5		3.78	2.91	2.35
Irfppy	548	n.d.	17 ± 1.2		1.32	17.4	5.83
ZIrfppy	545	n.d.	3.0 ± 0.81	2.9	0.0328	91.5	296
ZIrfppy + Zn^{2+} [i]	570	n.d.	8.7 ± 1.4		1.23	7.07	7.42
Irppy	582	n.d.	9.0 ± 0.97		0.813	3.69	11.9
ZIrppy	575	n.d.	9.4 ± 1.8	0.50	0.516	18.2	17.6
ZIrppy + Zn^{2+} [i]	610	n.d.	4.7 ± 0.59		0.945	4.97	10.1
Irbtp	590	1395	1.0 ± 0.77		2.09	0.479	4.74
ZIrbtp	592	1338	0.84 ± 0.40	0.36	5.53	0.152	1.80
ZIrbtp + Zn^{2+} [i]	649	1424	0.30 ± 0.17		0.00973[j]	0.0308	1.02
IrOMe	655	n.d.	0.21 ± 0.045		0.00395[j]	53.1	2530
ZIrOMe	651	n.d.	0.32 ± 0.31	0.75	0.00596[j]	53.7	1670
ZIrOMe + Zn^{2+} [i]	675	n.d.	0.24 ± 0.11		0.00169[j]	142	5900

[a] 10 μM phosphorescence zinc sensor in acetonitrile solutions, 298 K. [b] λ_{ex} = 393 (ZIrdCF3), 359 (ZIrdfppy), 362 (ZIrfppy), 377 (ZIrppy), 412 (ZIrpbt), 434 (ZIrbtp), and 377 nm (ZIrOMe). [c] Vibronic spacing of the room-temperature phosphorescence spectrum; n.d. = no vibronic structure. [d] Relative phosphorescence (photoluminescence) quantum yield with respect to fluorescein standard (0.1 N NaOH; Φ = 0.79). Measurements were conducted in triplicate. Fresh sample solutions (acetonitrile) were thoroughly degassed through the repeated vacuum−freeze−thaw cycles. [e] Dynamic range: DR = Φ/Φ_0, where Φ and Φ_0 are the phosphorescence quantum yields of the zinc-bound and zinc-free forms, respectively. [f] Phosphorescence lifetimes observed at λ_{em} = 498 (ZIrdCF3), 520 (ZIrdfppy), 550 (ZIrfppy), 575 (ZIrppy), 525 (ZIrpbt), 590 (ZIrbtp), and 650 nm (ZIrOMe). [g] Radiative rate constant: $k_r = \Phi/\tau_{obs}$. [h] Nonradiative rate constant: $k_{nr} = (1 - \Phi)/\tau_{obs}$. [i] 3 equiv of $Zn(ClO_4)_2$. [j] Data obtained from the picosecond TCSPC experiments.

used for the preparation of the C∧N ligands. The cyclometalated chloride-bridged Ir(III) dimers, $[Ir(C\wedge N)_2(\mu\text{-}Cl)]_2$, were obtained by the Nonoyama reaction.[81] A 1,10-phenanthroline ligand linked to a zinc-chelating DPA moiety was obtained through a procedure reported previously.[61] Substitution of the chlorides in $[Ir(C\wedge N)_2(\mu\text{-}Cl)]_2$ with the

dx.doi.org/10.1021/ja3123202 | J. Am. Chem. Soc. 2013, 135, 4771−4787

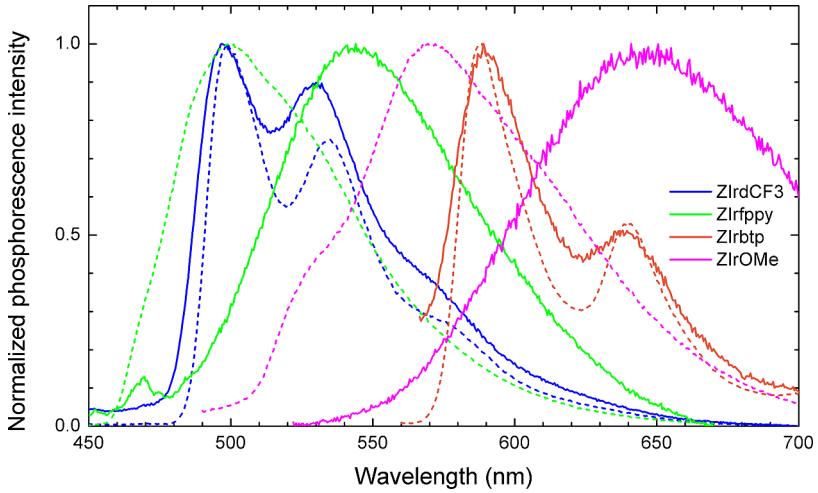

Figure 2. Normalized phosphorescence spectra of ZIrdCF3 (blue), ZIrfppy (green), ZIrbtp (orange), and ZIrOMe (magenta) in acetonitrile acquired at 79 K (dashed lines) and 270 K (solid lines). Concentration = 10 μM. Photoexcitation wavelengths: 393 (ZIrdCF3), 362 (ZIrfppy), 434 (ZIrbtp), and 377 nm (ZIrOMe).

Table 2. Summary of TD-UB3LYP Calculation Results from Models of the Phosphorescence Sensors[a]

compound	T_1 state energy (eV)	participating MOs (expansion coefficient)	position of LUMO(+n)[b]	DR[c]
ZIrdfppy	2.75 (451 nm)	HOMO−7→LUMO+1 (0.39) HOMO−4→LUMO+1 (0.46)	N∧N ligand	31
ZIrdCF3	2.62 (473 nm)	HOMO→LUMO+1 (0.42)	N∧N + C∧N ligands	12
ZIrfppy	2.71 (458 nm)	HOMO→LUMO (0.46)	N∧N ligand	2.9
ZIrpbt	2.51 (494 nm)	HOMO→LUMO+2 (0.58)	C∧N ligand	0.91
ZIrppy	2.55 (485 nm)	HOMO→LUMO (0.69)	N∧N ligand	0.50
ZIrbtp	2.15 (577 nm)	HOMO→LUMO+2 (0.62)	C∧N ligand	0.36
ZIrOMe	2.28 (543 nm)	HOMO→LUMO (0.70)	N∧N ligand	0.75

[a]B3LYP/LANL2DZ:6-31+G(d,p)/C-PCM (acetonitrile)//UB3LYP/LANL2DZ:6-31+G(d,p)/C-PCM (acetonitrile). [b]LUMO constructing T_1 state (n = 0, 1, or 2). Refer to Figure 3. [c]Experimental dynamic range.

DPA-appended 1,10-phenanthroline ligand, followed by metathesis with NH_4PF_6, afforded the sensors. Reference compounds lacking the DPA appendage were obtained using 1,10-phenanthroline through an identical method. The compounds were thoroughly purified and analyzed by standard procedures to verify their structures. Synthetic procedures and spectroscopic data for the identification of the compounds are described in the Experimental Section and in the Supporting Information (SI, Figures S1−S32). The cationic Ir(III) complexes were highly soluble in acetonitrile and buffered aqueous solutions (pH 7.4, 50 mM HEPES containing 100 mM KCl and 5 vol % DMSO) up to concentrations of 10 mM and 100 μM, respectively.

Photophysical Properties of the Phosphorescence Zinc Sensors. UV−vis absorption and phosphorescence spectra of the phosphorescence zinc sensors were recorded in acetonitrile (Figure 1). The sensors exhibited strong absorption at 250−300 nm (ε = 4 × 10^4−7 × 10^4 M^{-1} cm^{-1}) due to the spin-allowed singlet transitions of the C∧N ligands and 1,10-phenanthroline. The singlet metal-to-ligand charge-transfer (^{1}MLCT) absorption band appeared at >350 nm (ε < 1 × 10^4 M^{-1} cm^{-1}),[82] with a peak position that depended strongly on the identity of the C∧N ligand. The electron-rich C∧N ligands, such as the OMe ligand, produced a bathochromic shift in the MLCT transition band.

The peak wavelengths of the MLCT bands increased in the order ZIrdCF3 (356 nm) < ZIrdfppy (365 nm) = ZIrfppy (365 nm) < ZIrpbt (374 nm) < ZIrppy (375 nm) < ZIrbtp (434 nm) < ZIrOMe (440 nm). This trend was consistent with the shift in the phosphorescence peak wavelength (λ_{em}). As shown in Figure 1, an increase in the electron density produced a pronounced red shift from 498 (ZIrdCF3) to 651 nm (ZIrOMe). These spectral shifts were due to the inductive destabilization of the dπ orbital of Ir and C∧N ligands, corroborated by the observation of cathodic shifts in the Ir^{IV}/Ir^{III} redox potentials (*vide infra*). The zinc sensors were weakly phosphorescent in the absence of zinc ions. Photoluminescence quantum yields (Φ) were determined relative to the fluorescein standard and fell within the range 0.32−12%. Photophysical characterization data for the phosphorescence zinc sensors and their reference compounds are listed in Table 1.

The Ir(III) complexes displayed different vibronic structures in their phosphorescence spectra, depending on the ligand structures. As shown in Figure 1, ZIrdCF3, ZIrpbt, and ZIrbtp displayed distinct vibronic progressions, with vibronic spacings ($\Delta\nu$) of 1394, 1395, and 1338 cm^{-1}, respectively. The $\Delta\nu$ value for ZIrdfppy was determined to be 1367 cm^{-1} after deconvolution using a Lorentzian envelope. The $\Delta\nu$ values corresponded to the vibrational frequencies of the C=C and C=N bonds in the C∧N ligand.[83] The vibronic progression of ZIrdCF3 and ZIrbtp became more apparent at 79 K, but no spectral shifts were observed (Figure 2). These phosphorescence signatures were characteristic of the ligand-centered (LC) transition.[82,84,85] By contrast, ZIrfppy, ZIrppy, and ZIrOMe displayed structureless phosphorescence spectra at room temperature, suggesting that their phosphorescence was

dx.doi.org/10.1021/ja3123202 | J. Am. Chem. Soc. 2013, 135, 4771−4787

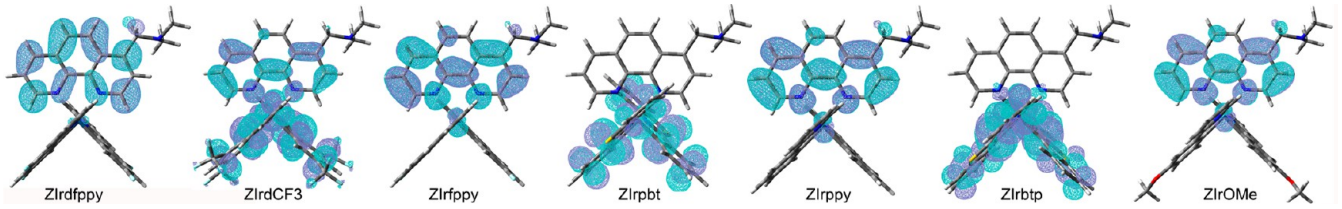

Figure 3. Calculated geometry and isosurface plot (0.04 e Å^{-3}) of the LUMO(+n) (n = 0, ZIrfppy, ZIrppy, and ZIrOMe; n = 1, ZIrdfppy and ZIrdCF3; n = 2, ZItpbt and ZIrbtp).

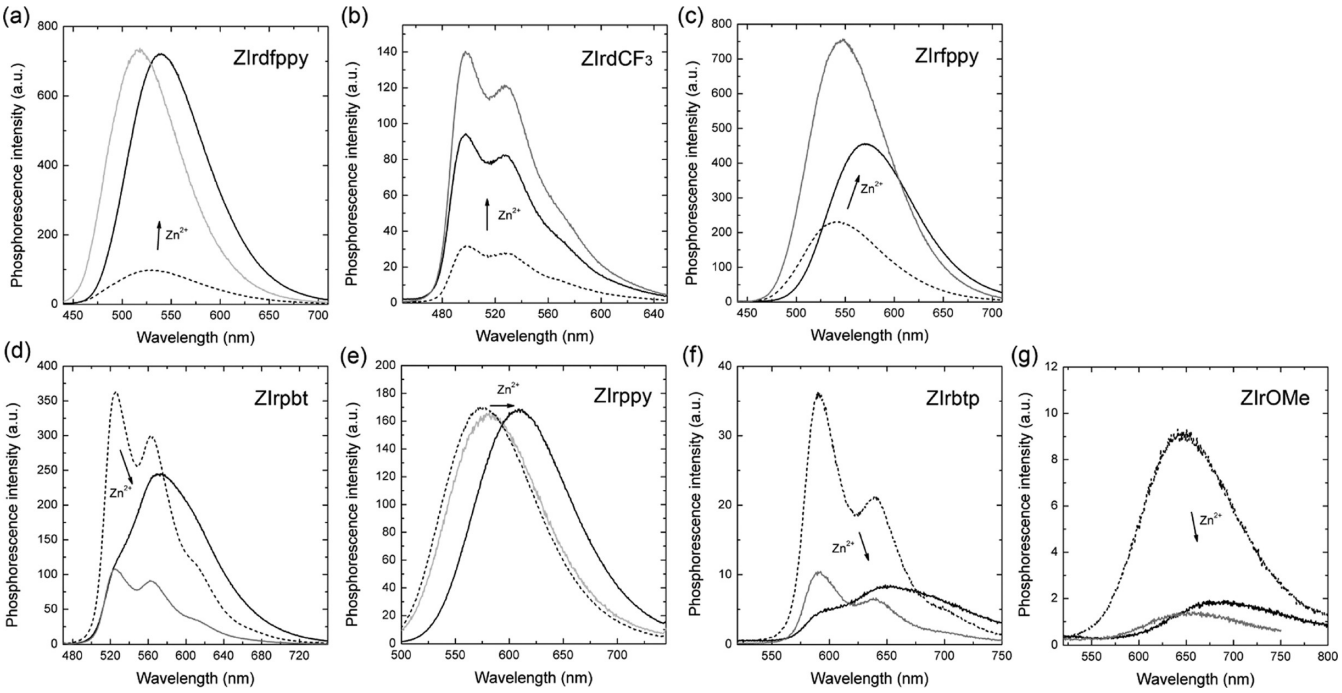

Figure 4. Phosphorescence spectra of the 10 μM zinc sensors (Ar-saturated CH_3CN) in the absence (dashed black lines) or presence (solid black lines) of zinc ions (3 equiv of $Zn(ClO_4)_2$). The phosphorescence spectra of the reference compounds are plotted for comparison (10 μM, gray lines). Photoexcitation wavelengths: 393 (ZIrdCF3), 359 (ZIrdfppy), 362 (ZIrfppy), 377 (ZIrppy), 412 (ZIrpbt), 434 (ZIrbtp), and 377 nm (ZIrOMe).

dominated by a MLCT or a ligand-to-ligand charge-transfer (LLCT) transition.[67,77−79,82,86,87] The phosphorescence spectra of ZIrfppy and ZIrOMe displayed significant hypsochromic shifts at lower temperatures, as expected for the charge-transfer emission (Figure 2). The phosphorescence sensors were categorized into two groups on the basis of the phosphorescence properties of the complexes: the LC (ZIrdCF3, ZIrpbt, and ZIrbtp) and the MLCT/LLCT (ZIrfppy, ZIrppy, and ZIrOMe) groups. ZIrdfppy displayed properties that were intermediate between the properties of the two groups. This categorization was weakly correlated with the phosphorescence peak wavelength.

Influence of the Coulombic Barrier. The influence of the Coulombic barrier on phosphorescence was explored by performing DFT/TD-DFT calculations. Geometry optimization was conducted using the B3LYP/LANL2DZ:6-31+G(d,p) method along with the conductor-like polarizable continuum model (C-PCM) of solvent effects. The pyridine moiety in the DPA appendage was truncated because it contributed negligibly to the electronic transitions of the Ir(III) complexes. Electronic transition energies were calculated using the TD-UB3LYP/LANL2DZ:6-31+G(d,p)/C-PCM (acetonitrile) method, and the results are summarized in Table 2.

The ordering of the calculated triplet state (T_1) energies was roughly consistent with ordering determined from the experimentally observed ^{1}MLCT absorption bands (Figure 1), despite the neglect of the exchange energy (i.e., $E_{singlet} - E_{triplet}$) in the computational treatment. Because intersystem crossing in typical cyclometalated Ir(III) complexes is ultrafast,[88,89] the Coulombic barrier could be located by identifying the ligand bearing a LUMO(+n) that contributed to the T_1 state. As shown in Figure 3, the LUMO(+n) isosurfaces of ZIrdCF3, ZIrpbt, and ZIrbtp were distributed over the C∧N ligands. This result suggested that the Coulombic barrier would be minimal in the processes of PeT from DPA to the Ir^{IV} center. By contrast, the LUMO(+n) isosurfaces of ZIrdfppy, ZIrfppy, ZIrppy, and ZIrOMe were mainly localized in the 1,10-phenanthroline, indicating the presence of a Coulombic barrier. Interestingly, the former (i.e., ZIrdCF3, ZIrpbt, and ZIrbtp) and the latter groups (i.e., ZIrdfppy, ZIrfppy, ZIrppy, and ZIrOMe) were characterized as yielding LC or MLCT/LLCT phosphorescence, respectively (Figures 1 and 2).

Having predicted the position of the Coulombic barriers, we attempted to correlate their effects with the DR values. The phosphorescence spectra of the zinc-free and zinc-bound forms of the sensors were collected (Figure 4). A phosphorescence

dx.doi.org/10.1021/ja3123202 | J. Am. Chem. Soc. 2013, 135, 4771−4787

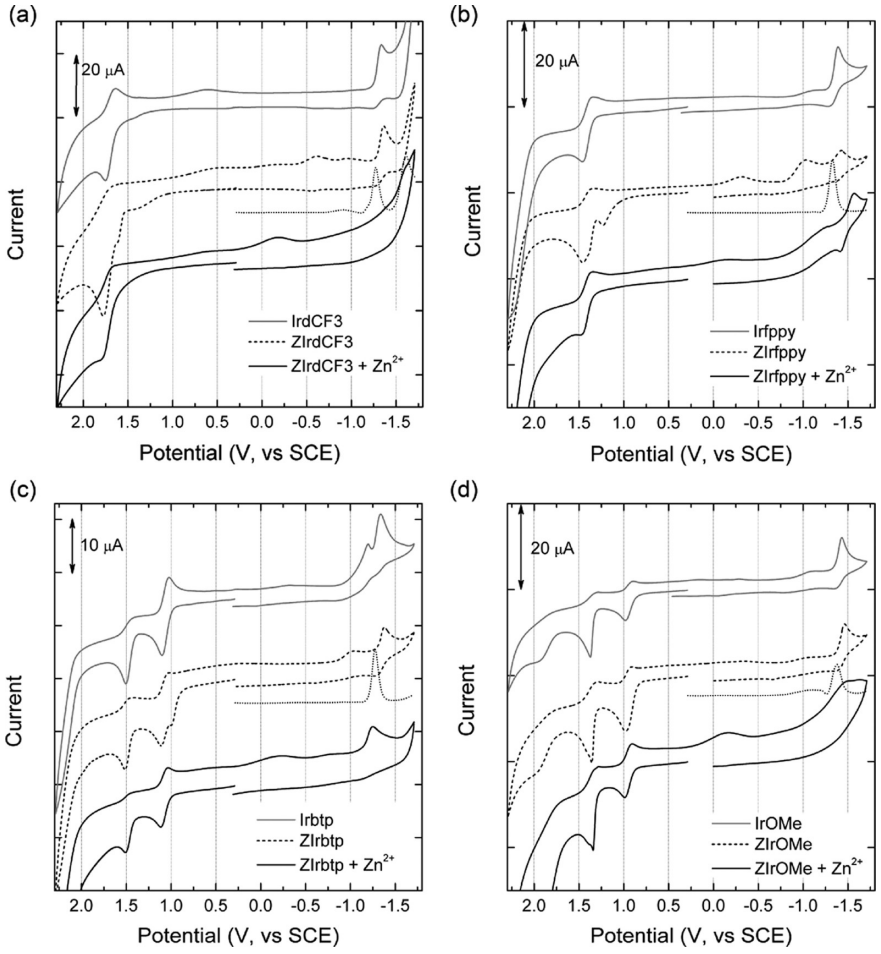

Figure 5. Cyclic voltammograms of ZIrdCF3 (a), ZIrfppy (b), ZIrbtp (c), and ZIrOMe (d) in the absence (dashed lines) or presence (solid lines) of zinc ions (2 equiv $Zn(ClO_4)_2$). Gray lines indicate the cyclic voltammograms of the reference compounds. Dotted lines indicate differential pulse voltammograms of the zinc-free sensors. Conditions: a Pt wire counter electrode and a Pt disc working electrode; a $Ag/AgNO_3$ pseudo reference electrode; deaerated CH_3CN solutions containing 0.10 M Bu_4NPF_6 and a 1.0 mM zinc sensor. Scan rates: 100 mV/s for cyclic voltammetry and 4 mV/s for differential pulse voltammetry.

turn-on response was observed in ZIrdfppy, ZIrdCF3, and ZIrfppy upon the addition of zinc ions (3 equiv $Zn(ClO_4)_2$), whereas ZIrppy displayed a negligible change in the phosphorescence intensity. By contrast, zinc coordination of ZIrpbt, ZIrbtp, and ZIrOMe led to a weak phosphorescence turn off. The corresponding DR values were calculated from the Φ values determined for the zinc-free and zinc-bound forms because the UV−vis absorption spectra were insensitive to the presence of zinc ions (SI, Figure S33). As listed in Table 1, ZIrdfppy (31), ZIrdCF3 (12), and ZIrfppy (2.9) displayed DR values larger than 1, whereas the other Ir(III) complexes displayed DR values smaller than 1. The DR values were apparently weakly correlated with the Coulombic barrier. For example, ZIrdfppy, the DR value of which was predicted to be small due to the presence of a Coulombic barrier, yielded the greatest DR value (31). Phosphorescence turn-off was observed from ZIrpbt (0.91) and ZIrbtp (0.36), although the temperature-dependent phosphorescence spectra and the TD-DFT calculations predicted a minimal effect on the Coulombic barrier. These results indicated that PeT from the DPA appendage to the photoexcited Ir^{IV} center was unaltered by the Coulombic barrier. Therefore, coordinative disposition of ligands in the heteroleptic Ir(III) complex may be insignificant to the extent of phosphorescence modulation.

Interestingly, a bathochromic shift was observed upon zinc coordination, as shown in Figure 4. The spectral shifts ($\Delta\lambda_{em} = \lambda_{em}(zinc) - \lambda_{em}(free)$) were 529 (ZIrdfppy), 805 (ZIrfppy), 998 (ZIrppy), and 546 cm^{-1} (ZIrOMe). These complexes were characterized by pronounced MLCT/LLCT phosphorescence (Figures 1 and 2). The chromic shifts arose from the sensitivity of the charge-transfer phosphorescence to the surrounding medium;[61,76] for example, the presence of a positively charged Zn^{2+} ion altered the phosphorescence properties. The same bathochromic effects were observed in the presence of strong Lewis acids, such as H^+, Cd^{2+}, and Sc^{3+} ions (SI, Figure S34).

E^*_{red} Engineering in the Phosphorescence Zinc Sensors. Figure 5 depicts the cyclic and the differential pulse voltammograms of ZIrdCF3, ZIrfppy, ZIrbtp, and ZIrOMe. The voltammograms of the other Ir(III) complexes are shown in SI, Figure S35. The cyclic voltammograms of the sensors were essentially indistinguishable from the voltammograms of the reference compounds, except for the irreversible oxidation due to the DPA group (1.28 V, vs SCE).[61] The DPA oxidation disappeared within the experimental window (<2.0 V, vs SCE) upon zinc coordination. This effect was ascribed to a zinc-induced anodic shift. In addition to the DPA oxidation, reversible or quasi-reversible waves due to the Ir^{IV}/Ir^{III} redox process were observed at 0.94−1.72 V (vs SCE) (Table 3). The

dx.doi.org/10.1021/ja3123202 | J. Am. Chem. Soc. 2013, 135, 4771−4787

Table 3. Electrochemical and Photoelectrochemical Data for the Phosphorescence Sensors

compound	ΔE_{00}[a]	$E^{\circ}(Ir^{IV}/Ir^{III})$ (V, SCE)[b]	E°_{red} (V, SCE)[c]	E^{*}_{red} (V, SCE)[d]	$-\Delta G_{PeT}$ (eV)[e]	k_{PeT} ($\times 10^6$ s^{-1})[f]
ZIrdfppy	2.77	1.56 (r)	−1.30	1.47	0.19	15.6
ZIrdCF3	2.71	1.72 (qr)	−1.27	1.44	0.16	2.14
ZIrfppy	2.65	1.46 (r)	−1.32	1.33	0.05	1.44
ZIrpbt	2.52	1.39 (r)	−1.31	1.21	−0.07	n.a.
ZIrppy	2.52	1.25 (r)	−1.36	1.16	−0.12	n.a.
ZIrbtp	2.37	1.08 (r)	−1.28	1.09	−0.19	n.a.
ZIrOMe	2.37	0.94 (r)	−1.38	0.99	−0.29	n.a.

[a]Optical band gap energy determined at the intersection of the UV−vis absorption and phosphorescence spectra. Conditions: 10 μM phosphorescence zinc sensor in acetonitrile, 298 K. [b]Determined by cyclic voltammetry. Conditions: scan rate = 100 mV/s; 1.0 mM sensor in Ar-saturated acetonitrile containing a 0.10 M Bu_4NPF_6 supporting electrolyte; Pt wire counter electrode and Pt disc working electrode; $Ag/AgNO_3$ couple as the pseudo reference electrode. r = reversible wave, qr = quasi reversible wave. [c]Determined by differential pulse voltammetry. Conditions: scan rate = 4 mV/s; 1.0 mM sensor in Ar-saturated acetonitrile containing a 0.10 M Bu_4NPF_6 supporting electrolyte; Pt wire counter electrode and Pt disc working electrode; $Ag/AgNO_3$ couple as the pseudo reference electrode. [d]Excited-state reduction potential $E^{*}_{red} = E^{\circ}_{red} + \Delta E_{00}$. [e]Driving force for PeT: $-\Delta G_{PeT} = -e[E^{\circ}_{ox}(DPA) - E^{*}_{red}(Ir\ complex)] + w_p$; the electrostatic interaction energy in the radical ion pair (w_p) was ignored in polar solvent. [f]Rate constant for PeT: $k_{PeT} = (DR - 1)/\tau_{obs}$, where τ_{obs} is the phosphorescence lifetime of the reference compound. τ_{obs} values are listed in Table 1. n.a. = no PeT.

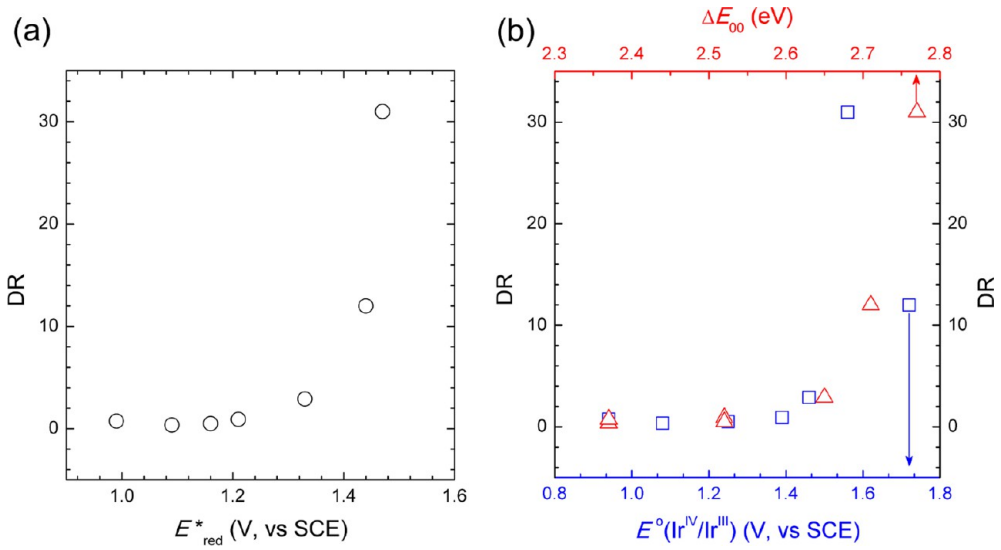

Figure 6. Photoelectrochemical parameters that affected the dynamic range (DR). (a) Correlation of DR and E^{*}_{red}. (b) Relationships between DR and ΔE_{00}, and the redox potentials of the Ir center ($E^{\circ}(Ir^{IV}/Ir^{III})$).

Ir^{IV}/Ir^{III} redox potentials were cathodically shifted for higher C∧N ligand electron densities. The ground-state reduction potentials (E°_{red}) were determined by differential pulse voltammetry. The E°_{red} values, −1.38 to −1.27 V (vs SCE), corresponded to the reductions of the 1,10-phenanthroline or C∧N ligands.[90−93] As in the Ir^{IV}/Ir^{III} redox process, the reduction potentials exhibited cathodic shifts for higher C∧N ligand electron densities. The excited-state reduction potentials (E^{*}_{red}) were calculated according to the relationship $E^{*}_{red} = E^{\circ}_{red} + \Delta E_{00}$, where the optical band gap energy (ΔE_{00}) was determined using UV−vis absorption and phosphorescence spectra.[25,88,89] As listed in Table 3, the E^{*}_{red} values were successfully tuned by the C∧N ligand control over the range of 0.99−1.47 V (vs SCE). E^{*}_{red} was found to increase as the electron density of the C∧N ligands decreased, and ZIrdfppy displayed the greatest excited-state oxidizing power. This result predicted that phosphorescence emission from ZIrdfppy would be most effectively quenched by PeT, in good agreement with the experimental results (Figure 4 and Table 1).

PeT Control and Its Correlation with the Dynamic Range. The optical and electrochemical properties (ΔE_{00}, $E^{\circ}_{ox}(Ir^{IV}/Ir^{III})$, and E^{*}_{red}) of the zinc sensors were next correlated with the DR values. Figure 6a shows that the DR remained below 1 until E^{*}_{red} < 1.2 V (vs SCE), and the DR value began to increase at $E^{*}_{red} \approx 1.2$ V. This potential coincided with the DPA oxidation potential (1.28 V, vs SCE), suggesting occurrence of oxidative electron transfer from DPA. PeT is allowed at E^{*}_{red} > 1.2 V (vs SCE), according to the prediction of a positive driving force $[E^{*}_{red}(Ir\ complex) - E^{\circ}_{ox}(DPA)]>0$ for exergonic electron transfer (Figure 7).[94,95] Plots of the DR values against $E^{\circ}_{ox}(Ir^{IV}/Ir^{III})$ and ΔE_{00} further revealed that ΔE_{00}, rather than $E^{\circ}_{ox}(Ir^{IV}/Ir^{III})$, determined the DR (Figure 6b). This finding provides important design criteria: band gap energy control is more effective than electrochemical control in tuning the extent of PeT in these Ir(III) complexes. Furthermore, the results demonstrated the risks associated with predicting excited-state redox processes, such as PeT, on the basis of the ground-state redox potentials.

The correlation between the DR and PeT was quantified according to the Rehm−Weller terminology.[96] The driving force for PeT ($-\Delta G_{PeT}$) was calculated using the relationship $-\Delta G_{PeT} = -e[E^{\circ}_{ox}(DPA) - E^{*}_{red}(Ir\ complex)] + w_p$ (Table 3), where the electronic interaction energy (w_p) was neglected in polar solvents, such as acetonitrile.[51,97] Apparently, DR values

dx.doi.org/10.1021/ja3123202 | J. Am. Chem. Soc. 2013, 135, 4771−4787

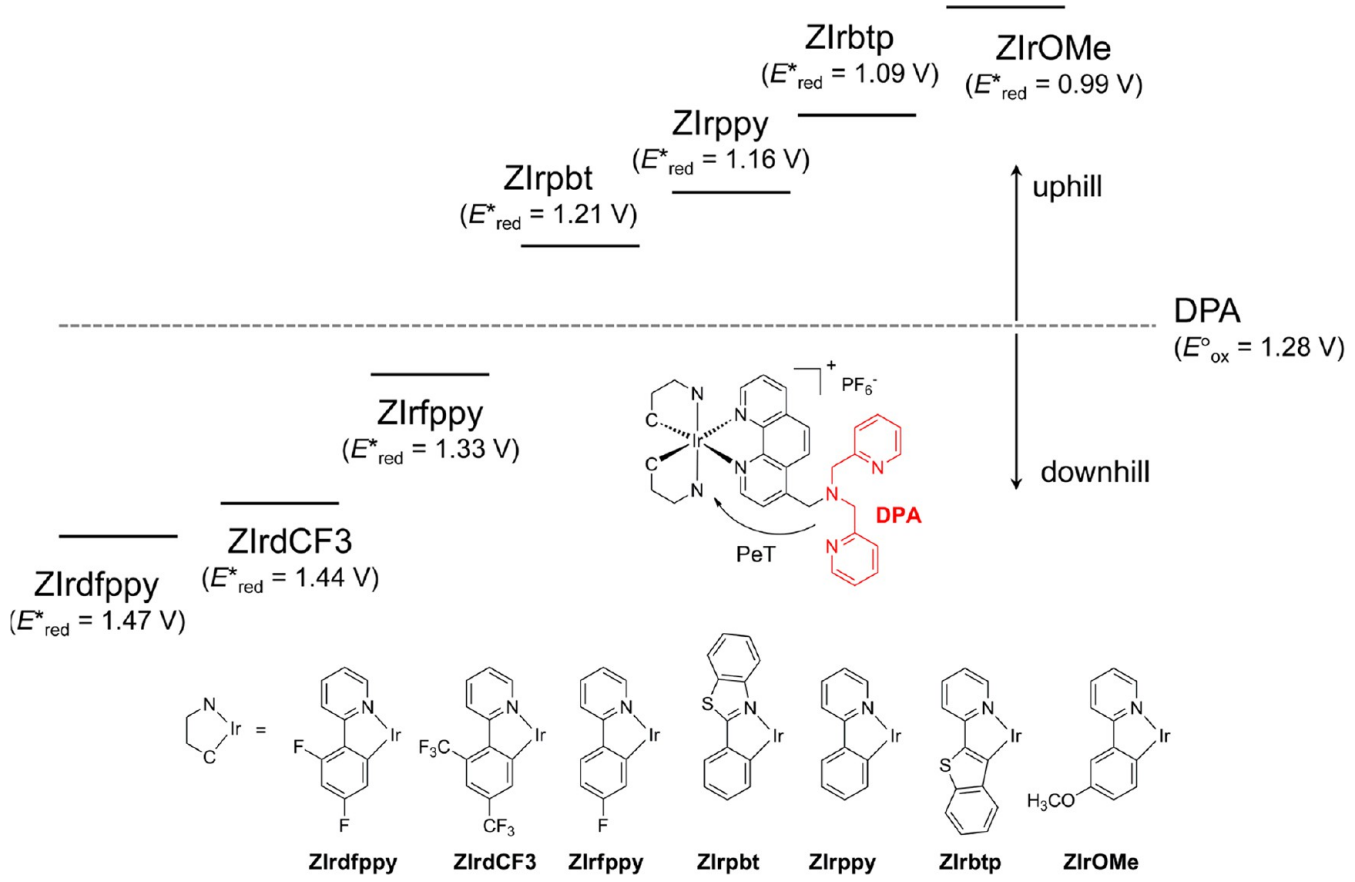

Figure 7. Schematic representation of the relative position of the ground-state oxidation potential (E°_{ox}) of DPA and the excited-state reduction potentials (E^*_{red}) of the Ir(III) complexes (vs SCE).

exceeding 1 were observed for Ir(III) complexes with $-\Delta G_{PeT} > 0$ (Figure 8), and the value increased in proportion to $-\Delta G_{PeT}$. This correlation convincingly supported a mechanism in which PeT was the dominant process contributing to the phosphorescent response to zinc ions. Thus, it is anticipated that larger DR values may be attained using (1) a wide band gap (i.e., large ΔE_{00}) and (2) an electron deficient (i.e., large E°_{red}) ligand. This design rationale suggests that *N*-heterocyclic carbene ligands[98,99] would be ideal candidates for improving the DR values.

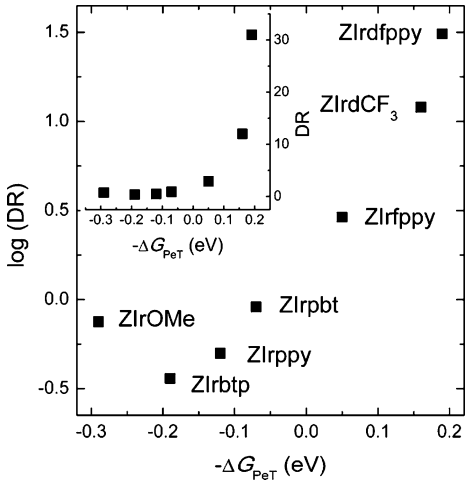

Figure 8. A log plot of the dynamic range (DR) as a function of the driving force for photoinduced electron transfer ($-\Delta G_{PeT}$). Inset: a linear plot of DR as a function of $-\Delta G_{PeT}$.

The overall rate constant for PeT (k_{PeT}) was calculated according to the relationship $k_{PeT} = (DR - 1)/\tau_{obs}$,[94,100] where τ_{obs} is the phosphorescence lifetime of the reference compound without the DPA appendage. The k_{PeT} values were 15.6×10^6 (ZIrdfppy), 2.14×10^6 (ZIrdCF3), and 1.44×10^6 s^{-1} (ZIrfppy), 2 orders of magnitude larger than the k_r values (Table 1). As shown in Figure 9, the logarithm of the k_{PeT} values increased in proportion to $-\Delta G_{PeT}$, implying that PeT in the phosphorescence sensors occurred in the Marcus-normal region.[101,102] This finding provides guidelines for improving PeT (that is, enhancing the phosphorescence response): larger PeT driving forces yield greater DR values. Because the driving force for PeT ($-\Delta G_{PeT}$) is tunable through controlling molecular parameters, such as electrochemical potentials and band gap energies, further improvement in DR values is feasible. This principle contrasts with the properties of PeT that occur in the Marcus-inverted region. This region favors smaller driving forces, as in the case of a molecular dyad consisting of a Sn(IV) porphyrin and trinuclear Ru(III) cluster[103] or a mixture of *N*,*N*-dimethylaniline and coumarin compounds.[104]

The results demonstrated that PeT plays a dominant role in the phosphorescence response. The influence of the PeT modulation was monitored by comparing phosphorescence lifetimes (τ_{obs}) of the sensors in the presence or absence of zinc ions. Phosphorescence decay traces for a 50 μM phosphorescence zinc sensor (in deaerated acetonitrile) were recorded using time-correlated single photon counting (TCSPC)

dx.doi.org/10.1021/ja3123202 | J. Am. Chem. Soc. 2013, 135, 4771−4787

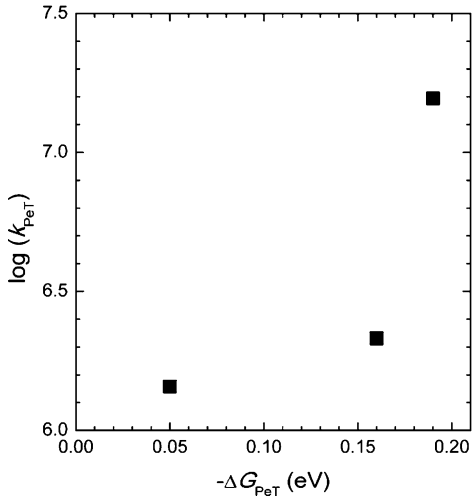

Figure 9. A log plot of the rate constant for photoinduced electron transfer (k_{PeT}) vs the driving force for photoinduced electron transfer ($-\Delta G_{PeT}$).

techniques after nano- or picosecond photoexcitation. The decay traces were fitted using an iterative nonlinear least-squares method with a monoexponential decay model, returning τ_{obs} values (Table 1). As expected, the τ_{obs} value for the zinc-free ZIrdCF3 was as short as 0.0512 ns, whereas the addition of zinc (3 equiv of $Zn(ClO_4)_2$) significantly increased the value to 5.35 μs (Figure 10a). The τ_{obs} values of the zinc-bound state were nearly identical to those of τ_{obs} (5.13 μs) for the reference compound. These similarities suggested that PeT was the dominant mechanism underlying phosphorescence quenching in the zinc-free state. The rate constant for the overall nonradiative decay (k_{nr}) consequently decreased from 1.93×10^7 to 1.55×10^5 s^{-1} upon zinc coordination. The latter rate constant was comparable to k_{nr} (1.54×10^5 s^{-1}) for the reference compound. Similarly, ZIrfppy displayed a large increase in τ_{obs} upon zinc coordination (Figure 10b). In contrast with the ZIrdCF3 and ZIrfppy complexes, sensors lacking PeT (ZIrbtp and ZIrOMe) showed the opposite trend (Figure 10c,d). The τ_{obs} value for the zinc-free ZIrbtp was as large as 5.53 μs because the quenching effects of PeT were absent. The addition of zinc ions greatly decreased τ_{obs} to 9.73 ns. The same trend was observed for ZIrOMe, although the τ_{obs} values remained in the nanosecond regime. Recall that zinc coordination resulted in bathochromic shifts in the phosphorescence spectra irrespective of the DR values (Figure 4). Presumably, zinc binding directly influenced the triplet state of the Ir(III) complexes, thereby altering the overall depopulation processes both radiatively and nonradiatively. In fact, the rate constant associated with radiative decay (k_r) decreased upon

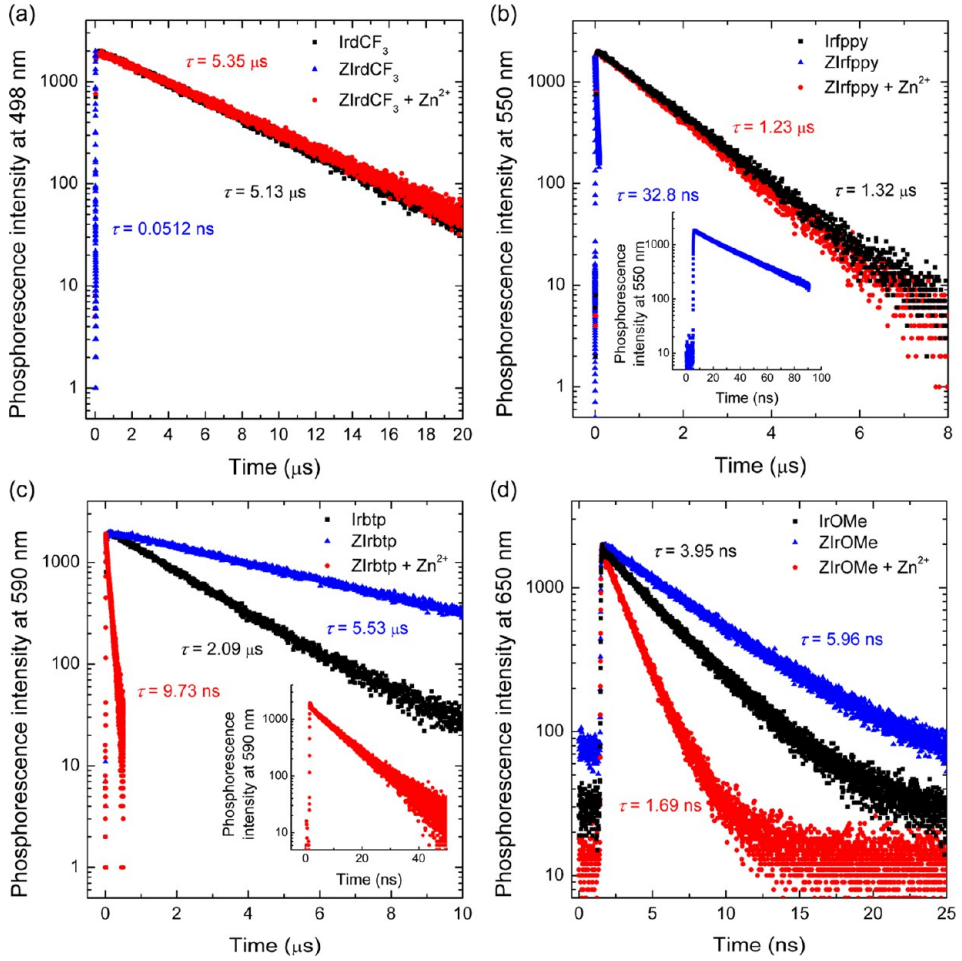

Figure 10. Phosphorescence decay traces of ZIrdCF3 (a), ZIrfppy (b), ZIrbtp (c), and ZIrOMe (d) in the presence (red) and absence (blue) of zinc ions and their reference compounds (black) after nanosecond or picosecond photoexcitation. Conditions: Ar-saturated CH_3CN solutions containing the compounds (50 μM) were photoexcited under 377 nm. Decay traces of other complexes are shown in SI, Figure S36.

dx.doi.org/10.1021/ja3123202 | J. Am. Chem. Soc. 2013, 135, 4771−4787

zinc binding (except in ZIrOMe, Table 1) which could not be explained in terms of the presence of PeT. Interestingly, a plot of log(DR) against $[\log(k_r/k_r^\circ) - \log(k_{nr}/k_{nr}^\circ)]$ (k_r and k_r° are the radiative rate constants in the presence or absence of zinc ions, respectively, and k_{nr} and k_{nr}° are the overall nonradiative rate constants in the presence or absence of zinc ions, respectively) displayed a linear relationship (Figure 11). This

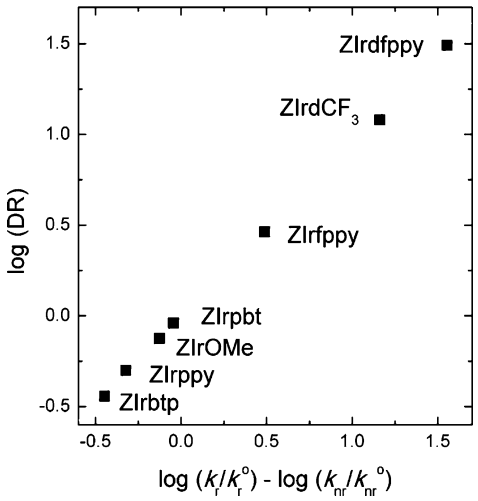

Figure 11. A log–log plot of the dynamic range (DR) as a function of $[\log(k_r/k_r^\circ) - \log(k_{nr}/k_{nr}^\circ)]$.

linear relationship suggests the presence of another zinc coordination effects other than PeT retardation. Although the mechanism underlying the radiative transition remains elusive, the results clearly demonstrate the dominant role of PeT in the phosphorescence turn-on response.

Biological Applications of the Phosphorescence Zinc Sensor. The mechanistic studies established that zinc-induced retardation of PeT is the key contributing factor to the phosphorescent response to zinc ions, and that the extent of PeT can be controlled by the C∧N ligand structure. These results suggested a demonstration of the biological utility of the series of phosphorescence zinc sensor. ZIrdCF3 was evaluated for its ability to indicate the presence of zinc ions via phosphorescence modulation in a buffered aqueous solution (50 mM HEPES + 100 mM KCl containing 5 vol % DMSO) at pH 7.4. We previously demonstrated the biological utility of the phosphorescence signaling of ZIrdfppy.[61] Despite a decrease in the DR value in aqueous solutions, the phosphorescence turn-on response to zinc ions was retained (SI, Figure S37a) and selective to zinc ions over other biologically relevant metal ions, including Na (1 mM), Mg (1 mM), K (100 mM), Ca (1 mM), Mn (10 μM), Fe (10 μM), Co (10 μM), and Cu (10 μM) (SI, Figure S37b).

Live HeLa cells were pretreated with a strong zinc chelator, 50 μM *N*,*N*,*N*′,*N*′-tetrakis(2-picolyl)ethylenediamine (TPEN)[17,27,30,33,105] for 5 min, followed by treatment with 10 μM ZIrdCF3 for 10 min. Weak punctate signals were observed in the cytoplasm under photoexcitation at 405 nm (Figure 12a). Subsequent incubation with 200 μM ZnPT (200 μM $ZnCl_2$ + 400 μM sodium pyrithione) for 10 min turned on the phosphorescence intensity, as shown in Figure 12b. Despite the spectral distortion, a comparison of the photoemission spectra of the HeLa cells acquired before and after the zinc treatment revealed ZIrdCF3 as responsible for the phosphorescence emission (Figure 12c).

As a final demonstration, we performed photoluminescence lifetime imaging microscope experiments for fixed HeLa cells (Figure 13). The HeLa cells were pretreated with 10 μM ZIrdCF3 (10 min), fixed with 4% formaldehyde, and subsequently mounted with Vectashield (Vector Labs). Photoluminescence lifetime images of the cells were recorded over an 80 μm × 80 μm sample area consisting of 200 × 200 pixels under photoirradiation from a 375 nm picosecond diode laser. Photoemission acquired through a 480–520 nm band-pass filter was deconvoluted using a triple-exponential decay model, returning fast (τ_1 = 1.2 ns), midrange (τ_2 = 5.5 ns), and slow (τ_3 = 310 ns) decay components (Table 4). The photoluminescence decay components of the cells additionally

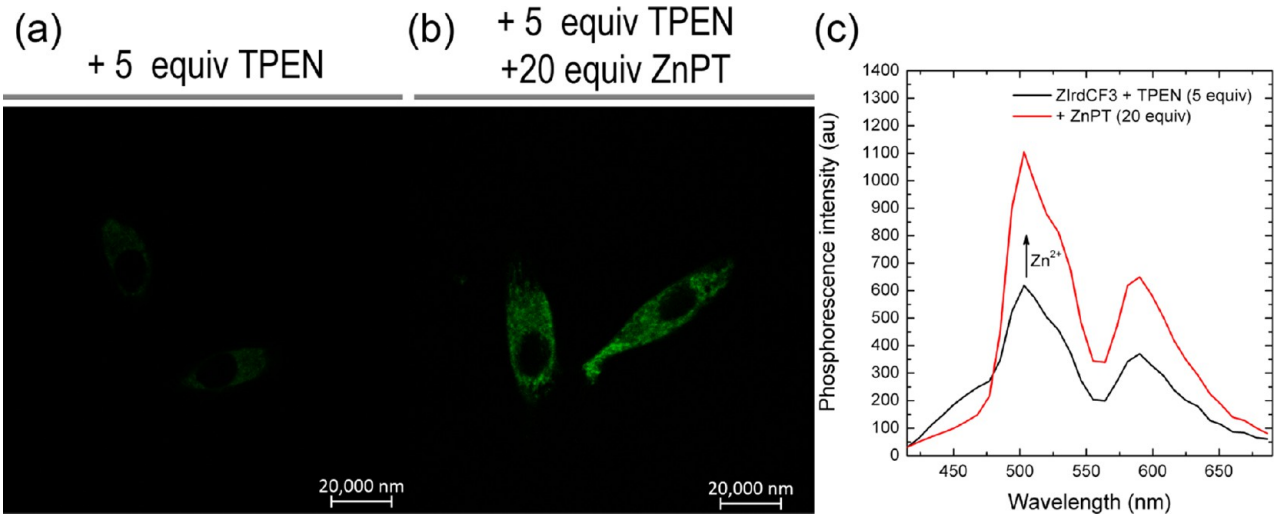

Figure 12. Phosphorescent visualization of intracellular zinc ions in live HeLa cells. (a) HeLa cells were pre-incubated with 50 μM TPEN (5 min), followed by 10 μM ZIrdCF3 (10 min). (b) The cells were further treated with 200 μM ZnPT (5 min). Phosphorescence images acquired in the 503 ± 5 nm emission channel are presented. The scale bars correspond to 20 μM. (c) Phosphorescence spectra acquired from the HeLa cells in panels a (black) and b (red). The cells were photoexcited at 405 nm, and phosphorescence emission was recorded through 30 emission channels from 410 to 691 nm.

dx.doi.org/10.1021/ja3123202 | J. Am. Chem. Soc. 2013, 135, 4771–4787

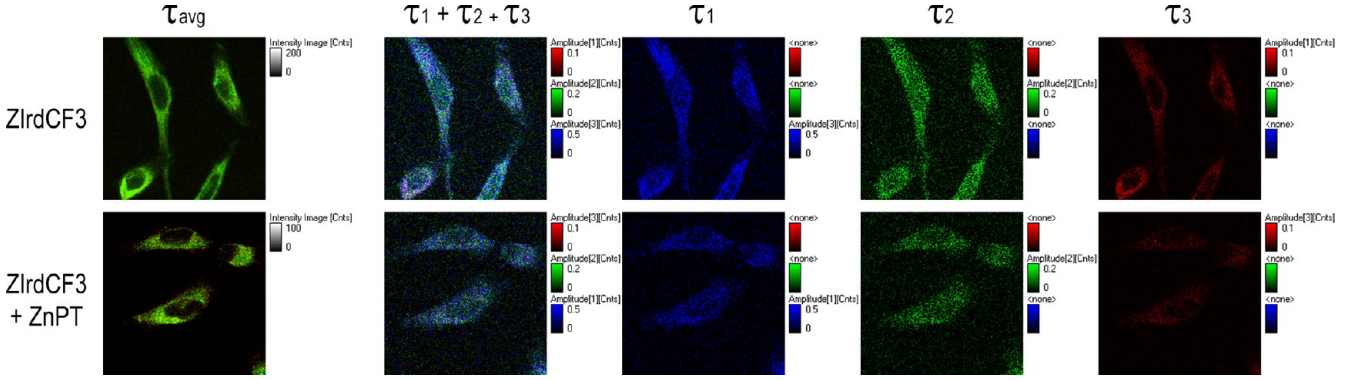

Figure 13. (a) Photoluminescence lifetime images (80 μm × 80 μm, λ_{ex} = 375 nm, λ_{obs} = 480−520 nm) of HeLa cells treated with 10 μM ZIrdCF3 (10 min). Cells in the lower panels were incubated with 100 μM ZnPT (5 min) prior to the ZIrdCF3 treatment. The images were analyzed using a three-exponential decay model: τ_{avg}, images constructed on the basis of the averaged photoluminescence lifetimes; τ_1, τ_2, and τ_3 indicate images constructed on the basis of the fast, midrange, and slow components, respectively; $\tau_1 + \tau_2 + \tau_3$, overlay images. Refer to Table 4 for the values of τ_1, τ_2, τ_3, and their amplitudes. The same intensity scale was applied to the cell images.

Table 4. Analysis of the Decay Traces of the Photoluminescence Lifetime Images of ZIrdCF3-Treated HeLa Cells before (−) and after (+) Incubation with Zinc Ions[a]

zinc	τ_{avg} (ns)[b]	A_1	τ_1 (ns)	A_2	τ_2 (ns)	A_3	τ_3 (ns)
−	269	73	1.2	22	5.5	5	310
+	425	72	1.0	22	5.1	6	450

[a]A triple-exponential decay model was applied: A, amplitude; τ, time constant. [b]$\tau_{avg} = \sum A_i\tau_i^2/\sum A_i\tau_i$ (i = 1−3).

treated with 100 μM ZnPT (5 min) were 1.0, 5.1, and 450 ns. An increase in the lifetime of the slow component (τ_3, red) resulted in a longer average photoluminescence lifetime (τ_{avg}) (Figure 13 and Table 4). The corresponding color changes in the τ_{avg} images were, therefore, attributed to zinc-induced lengthening of the photoluminescence lifetime, consistent with a mechanism involving PeT.

3. SUMMARY AND CONCLUSIONS

We synthesized a series of phosphorescence zinc sensors based on a cyclometalated heteroleptic Ir(III) complex that tethered the zinc-chelating di(2-picolyl)amino group. Seven cyclometalating ligands with a range of electron densities and band gap energies were incorporated into the sensors. Synthetic modulation of the electronic structures enabled a systematic investigation of the molecular factors governing the phosphorescence response to zinc ions. Steady-state and transient photoluminescence spectroscopic studies and electrochemical characterization were performed to determine the photophysical and photoelectrochemical properties of the complexes, including the ground- and excited-state redox potentials and the photoexcited state energies. Quantum chemical calculations based on TD-DFT predicted the position of the Coulombic barriers in the context of photoinduced electron transfer from the di(2-picolyl)amino group to the photoexcited Ir^{IV} center. The Coulombic barrier was found to negligibly influence the PeT process; however, the electron-transfer process strictly obeyed the Rehm−Weller equation. Phosphorescence quenching by nonradiative PeT processes was observed only when the excited-state reduction potentials of the Ir complexes were lower than the ground-state oxidation potential of the di(2-picolyl)amino moiety. The photoexcited state energy was the dominant parameter that determined the driving force for the PeT. Because the PeT occurred in the Marcus-normal region, large DR values were obtained for sensors with deep excited-state reduction potentials. These results point toward a viable strategy for further improving the DR, including the use of cyclometalating ligands with wide band gap energies and deep oxidation potentials, such as *N*-heterocyclic carbene ligands. Finally, the zinc detection capabilities of the phosphorescence sensor were assessed in buffered aqueous solutions at pH 7.4. As a useful example, the zinc sensor was used to visualize intracellular zinc ion distributions in HeLa cells using confocal laser scanning microscopy and photoluminescence lifetime imaging microscopy techniques. These results described here will provide useful guidelines for the future development of phosphorescence sensors.

4. EXPERIMENTAL SECTION

Materials and Synthesis. Commercially available chemicals, including 2-phenylpyridine and 2-phenylbenzothiazole, were used without further purification unless otherwise stated. All glassware and magnetic stirring bars were thoroughly dried in a convection oven. CH_2Cl_2 and THF were purified by filtering over anhydrous alumina columns prior to use. Reactions were monitored using thin-layer chromatography (TLC). Commercial TLC plates (silica gel 60 F_{254}, Merck Co.) were developed and the spots were visualized under UV illumination at 254 or 365 nm. Silica gel column chromatography was performed using silica gel 60 (particle size 0.063−0.200 mm, Merck Co.). ^{1}H and ^{13}C NMR spectra referenced to deuterated solvents were collected with a Bruker Ultrashield 400 plus NMR spectrometer. High-resolution mass spectra were recorded using a JEOL JMS-600W mass spectrometer. Elemental analysis was performed using an EA1110 or EA1112 (CE Instrument, Italy) for C, H, N, and S. The synthesis of 2-(2,4-difluorophenyl)pyridine and its μ-chloride-bridged Ir(III) dimer was performed according to the method reported previously.[106] ZIrdfppy and Irdfppy were prepared according to a method reported previously by us.[61]

4-Formyl-1,10-phenanthroline. 4-Methyl-1,10-phenanthroline (4.70 g, 24.2 mmol) and SeO_2 (8.30 g, 74.8 mmol) were suspended in 1,4-dioxane and H_2O (192 mL/8 mL), and the reaction mixture was refluxed for 1 day. After cooling, the solution was filtered through Celite and concentrated under vacuum. Alumina (basic, EMD) column purification with CH_2Cl_2:CH_3OH (19:1, v/v) gave a beige powder (1.88 g, 9.04 mmol) in a 37% yield. ^{1}H NMR (MeOD, 400 MHz): δ 7.70 (dd, J = 8.0, 4.4 Hz, 1H), 7.99 (d, J = 9.2 Hz, 1H), 8.01 (d, J = 4.4 Hz, 1H), 8.30 (dd, J = 8.0, 1.3 Hz, 1H), 9.03 (d, J = 9.2 Hz, 1H), 9.23 (dd, J = 4.4, 1.6 Hz, 1H), 9.47 (d, J = 4.4 Hz, 1H), 10.59 (s, 1H). ^{13}C NMR (MeOD, 100 MHz): δ 122.33, 123.89, 125.04, 126.82, 128.58, 129.70, 136.13, 136.82, 145.75, 147.47, 150.62, 151.04, 192.94.

dx.doi.org/10.1021/ja3123202 | J. Am. Chem. Soc. 2013, 135, 4771−4787

4-(Di(2-picolyl)aminomethyl)-1,10-phenanthroline. 4-Formyl-1,10-phenanthroline (1.66 g, 7.90 mmol), di(2-picolyl)amine (1.58 g, 7.90 mmol), and a catalytic amount of glacial acetic acid (two drops) were dissolved in anhydrous CH_3OH (150 mL), and the solution was refluxed for 0.5 h. The reaction mixture was cooled using an ice bath, and $NaBH_3CN$ (1.09 g, 17.3 mmol) was slowly added to the solution. The ice bath was removed, and the solution was stirred overnight at room temperature. Basic workup using a saturated aqueous sodium carbonate solution and subsequent extraction using CH_2Cl_2 was performed. The recovered organic layer was dried over anhydrous $MgSO_4$ and concentrated by vacuum. The crude product was subjected to silica gel column chromatography (CH_2Cl_2 to CH_2Cl_2:CH_3OH = 19:1, v/v), affording a sticky brown solid (1.00 g, 2.57 mmol) in a 33% yield. ^{1}H NMR (MeOD, 400 MHz): δ 3.71 (s, 4H), 4.03 (s, 2H), 6.92 (m, 2H), 7.23 (d, J = 8.0 Hz, 2H), 7.34−7.42 (m, 3H), 7.52 (d, J = 9.2 Hz, 1H), 7.61 (d, J = 4.4 Hz, 1H), 7.88 (d, J = 9.2 Hz, 1H), 7.98 (dd, J = 3.2, 1.6 Hz, 1H), 8.32 (m, 2H), 8.90 (d, J = 4.4 Hz, 1H), 8.93 (dd, J = 4.2, 1.6 Hz, 1H). ^{13}C NMR (MeOD, 100 MHz): δ 55.63, 60.44, 122.16, 122.76, 122.86, 123.15, 123.52, 125.86, 127.67, 128.04, 135.67, 136.39, 144.69, 146.15, 146.27, 148.95, 149.76, 150.03, 158.62.

Synthesis of the Cyclometalating Ligands. The Suzuki−Miyaura coupling of 2-bromopyridine (1 equiv) and aryl boronic acid (1.2 equiv) in the presence of tetrakis(triphenylphosphine)-palladium(0) (0.05 equiv) was employed for the synthesis. The reactants and the catalyst were dissolved in THF:2 N Na_2CO_3 (aq) (2:1, v/v) and refluxed for 1 day. The cooled reaction mixture was poured into water and extracted with CH_2Cl_2 (100 mL, four times), and the organic layer was dried over anhydrous $MgSO_4$ and concentrated. Purification by column chromatography on silica gel was performed to isolate the desired product.

2-(2,4-Bis(trifluoromethyl)phenyl)pyridine (dCF3). The method described above was applied to 2,4-bis(trifluoromethyl)phenyl boronic acid (2.00 g, 7.75 mmol). Silica gel column chromatography with n-hexane:CH_2Cl_2 = 5:1 (v/v) yielded a colorless liquid (1.55 g, 5.32 mmol) in an 82% yield. ^{1}H NMR ($CDCl_3$, 400 MHz): δ (dd, J = 12, 4.9 Hz, 1H), 7.45 (m, 1H), 7.66 (m, 1H), 7.80 (td, J = 7.7, 1.8 Hz, 1H), 7.88 (td, J = 7.7, 1.8 Hz, 1H), 8.03 (m, 1H), 8.72 (d, J = 4.9 Hz, 1H). ^{19}F NMR ($CDCl_3$, 376 MHz): δ −62.85 (m, 3F), −57.19 (m, 3F).

2-(4-Fluorophenyl)pyridine (fppy). The method described above was applied to (4-fluorophenyl boronic acid (2.03 g, 14.5 mmol). Silica gel column chromatography with n-hexane:CH_2Cl_2 = 7:1 (v/v) yielded a colorless oil (0.797 g, 4.60 mmol) in a 38% yield. ^{1}H NMR ($CDCl_3$, 400 MHz): δ 7.16 (m, 2H), 7.23 (dd, J = 13, 6.9 Hz, 1H), 7.68 (m, 1H), 7.75 (td, J = 8.0, 1.8 Hz, 1H), 7.96−8.00 (m, 2H), 8.68 (d, J = 4.8 Hz, 1H). ^{13}C NMR ($CDCl_3$, 100 MHz): δ 115.29, 115.51, 119.93, 121.87, 128.50, 128.58, 135.32, 136.59, 149.39, 156.01, 162.09, 164.56. HR MS (FAB, positive, m-NBA): calcd for $C_{11}H_9FN$ ([M+H]$^+$), 174.0719; found, 174.0719.

2-(Benzo[*b*]thiophen-2-yl)pyridine (btp). The method described above was applied to benzo[b]thien-2-yl boronic acid (2.00 g, 11.2 mmol). Silica gel column chromatography with n-hexane:CH_2Cl_2 = 5:1 (v/v) yielded a white solid (1.10 g, 5.21 mmol) in a 56% yield . ^{1}H NMR (400 MHz, $CDCl_3$): δ 7.23 (dd, J = 7.2, 4.8 Hz, 1H), 7.33−7.38 (m, 2H), 7.73 (m, 1H), 7.79 (m, 2H), 7.84 (m, 1H), 7.87 (m, 1H), 8.64 (td, J = 4.8, 0.8 Hz, 1H). HR MS (FAB, positive, m-NBA): calcd for $C_{13}H_{10}NS$ ([M+H]$^+$), 212.0534; found, 212.0534.

2-(3-Methoxyphenyl)pyridine (OMe). The method described above was applied to 3-methoxyphenyl boronic acid (1.00 g, 6.58 mmol). Silica gel column purification with n-hexane:CH_2Cl_2 = 3:1 (v/v) was performed, affording 0.789 g of a colorless oil (4.26 mmol, 77% yield). ^{1}H NMR ($CDCl_3$, 400 MHz): δ 3.89 (s, 3H), 6.97 (dd, J = 8.0, 2.4 Hz, 1H), 7.22−7.26 (m, 1H), 7.38 (t, J = 8.0 Hz, 1H), 7.54 (m, 1H), 7.60 (m, 1H), 7.71−7.75 (m, 2H), 8.69 (m, 1H). ^{13}C NMR ($CDCl_3$, 100 MHz): δ 55.59, 112.23, 115.34, 119.53, 120.96, 122.46, 129.94, 136.98, 141.09, 149.80, 157.49, 160.31. HR MS (FAB, positive, m-NBA): calcd for $C_{12}H_{11}NO$ ([M+H]$^+$), 186.0919; found, 186.0918.

Synthesis of the Chloride-Bridged Ir(III) Dimers. The method reported by Nonoyama et al. was employed for the synthesis.[81] Briefly, $IrCl_3{\cdot}nH_2O$ (Aldrich) and 4.47 equiv of a cyclometalating ligand were dissolved in 2-$EtOCH_2CH_2OH$:H_2O = 3:1 (v/v), and the solution was heated at 140 °C for 20 h. After cooling to room temperature, precipitates were filtered and thoroughly washed with acetone:ethanol = 1:1 (v/v). The precipitates were collected by dissolving with an excess amount of CH_2Cl_2, and the CH_2Cl_2 was removed under vacuum. The resulting powder was thoroughly dried and subjected to the next reaction without further purification.

[(dCF3)$_2$Ir(μ-Cl)]$_2$. $IrCl_3{\cdot}nH_2O$ (0.344 g, 1.15 mmol) and 2-(2,4-bis(trifluoromethyl)phenyl)pyridine (1.50 g, 5.15 mmol) were subjected to the Nonoyama protocol to yield a yellow powder (0.391g, 0.241 mmol) in a 42% yield.

[(fppy)$_2$Ir(μ-Cl)]$_2$. $IrCl_3{\cdot}nH_2O$ (0.386 g, 1.31 mmol) and 2-(4-fluorophenyl)pyridine (2.00 g, 11.5 mmol) were subjected to the Nonoyama protocol to yield a yellow powder (0.461 g, 0.403 mmol) in a 62% yield.

[(ppy)$_2$Ir(μ-Cl)]$_2$. $IrCl_3{\cdot}nH_2O$ (0.500 g, 1.67 mmol) and 2-phenylpyridine (Aldrich) (1.16 g, 7.48 mmol) were subjected to the Nonoyama protocol to yield a yellow powder (0.658 g, 0.614 mmol) in a 74% yield.

[(pbt)$_2$Ir(μ-Cl)]$_2$. $IrCl_3{\cdot}nH_2O$ (0.500 g, 1.67 mmol) and 2-phenylbenzothiazole (Aldrich) (1.58 g, 7.48 mmol) were subjected to the Nonoyama protocol to yield a reddish orange powder (0.900 g, 0.694 mmol) in an 83% yield.

[(btp)$_2$Ir(μ-Cl)]$_2$. $IrCl_3{\cdot}nH_2O$ (0.346, 1.16 mmol) and 2-(benzo[b]thiophen-2-yl)pyridine (1.10 g, 5.20 mmol) were subjected to the Nonoyama protocol to yield an orange powder (0.557 g, 0.430 mmol) in a 74% yield.

[(OMe)$_2$Ir(μ-Cl)]$_2$. $IrCl_3{\cdot}nH_2O$ (0.252 g, 0.845 mmol) and 2-(3-methoxyphenyl)pyridine (0.700 g, 3.78 mmol) were subjected to the Nonoyama protocol to yield an orange powder (0.280 g, 0.235 mmol) in a 56% yield.

Synthesis of the Phosphorescence Zinc Sensors and Their Reference Compounds. An anhydrous CH_2Cl_2 (30 mL) solution containing the chloride-bridged Ir(III) dimer ([(C∧N)$_2$Ir(μ-Cl)]$_2$) and 1.7 equiv of 4-(di(2-picolyl)aminomethyl)-1,10-phenanthroline or 1,10,-phenanthroline were refluxed for 6 h. The reaction mixture was cooled to room temperature, and NH_4PF_6 (15 equiv) was slowly added to the solution. After 12 h, the reaction mixture was filtered to remove residual NH_4PF_6 and concentrated under vacuum. The crude mixture was subjected to flash column chromatography on silica gel with CH_2Cl_2 to CH_2Cl_2:CH_3OH = 19:1. Further purification by preparative TLC techniques was performed to isolate the desired product.

ZIrdCF3. The synthesis method described above was applied to [(dCF3)$_2$Ir(μ-Cl)]$_2$ (0.200 g, 0.124 mmol) and 4-(di(2-picolyl)-aminomethyl)-1,10-phenanthroline (0.082 g, 0.210 mmol) to afford a yellow solid (0.153 g, 0.110 mmol) in an 89% yield. ^{1}H NMR ($CDCl_3$, 400 MHz): δ 3.97 (s, 4H), 4.51 (dd, J = 6.6, 1.6 Hz, 2H), 6.49 (d, J = 1.6 Hz, 2H), 7.10 (m, 2H), 7.13 (m, 1H), 7.23 (m, 1H), 7.44 (d, J = 7.8 Hz, 2H), 7.50 (dd, J = 5.7, 1.2 Hz, 1H), 7.61 (m, 3H), 7.75 (m, 2H), 7.83−7.91 (m, 4H), 8.05 (dd, J = 5.1, 1.4 Hz, 1H), 8.12 (d, J = 5.3 Hz, 1H), 8.21 (d, J = 9.2 Hz, 1H), 8.44 (m, 3H), 8.50 (m, 2H), 8.70 (dd, J = 8.3, 1.4 Hz, 1H). ^{13}C NMR (CD_3CN, 100 MHz): δ 119.40, 121.85, 122.24, 123.40, 124.55, 125.09, 125.35, 125.63, 126.00, 126.10, 126.82, 127.13, 127.44, 127.68, 129.59, 129.91, 131.09, 131.28, 131.53, 136.36, 139.18, 139.50, 139.58, 145.43, 146.01, 146.45, 148.97, 150.62, 150.74, 150.95, 151.57, 153.85, 158.58, 162.72. ^{19}F NMR ($CDCl_3$, 376 MHz): δ −73.52 (d, J = 714 Hz, 6F), −63.44 (m, 6F), −57.41 (m, 6F). HR MS (FAB, positive, m-NBA): calcd for $C_{50}H_{34}F_{12}IrN_8$ ([M−PF_6]$^+$), 1166.2393; found, 1166.2395. Anal. Calcd for $C_{51}H_{33}F_{18}IrN_7P$: C, 46.79; H, 2.54; N, 7.49. Found: C, 46.46; H, 2.62; N, 7.37.

IrdCF3. The synthesis method described above was applied to [(dCF3)$_2$Ir(μ-Cl)]$_2$ (0.176 g, 0.109 mmol) and 1,10-phenanthroline (33 mg, 0.19 mmol) to afford a yellow solid (97 mg, 88 μmol) in an 81% yield. ^{1}H NMR ($CDCl_3$, 400 MHz): δ 6.53 (s, 2H), 7.19 (m, 2H), 7.57 (dd, J = 5.8, 1.0 Hz, 2H), 7.77 (s, 2H), 7.87−7.92 (m, 4H), 8.09 (dd, J = 4.4, 1.4 Hz, 2H), 8.26 (s, 2H), 8.45 (d, J = 8.3 Hz, 2H), 8.72 (dd, J = 8.3, 1.4 Hz, 2H). ^{13}C NMR ($CDCl_3$, 100 MHz): δ

dx.doi.org/10.1021/ja3123202 | J. Am. Chem. Soc. 2013, 135, 4771−4787

119.89, 121.40, 122.06, 124.12, 124.34, 124.78, 125.59, 125.68, 126.26, 126.92, 127.74, 128.06, 129.12, 130.79, 131.05, 132.23, 139.24, 140.13, 144.66, 146.32. ^{19}F NMR ($CDCl_3$, 376 MHz): δ −73.23 (d, J = 710 Hz, 6F), −63.51 (m, 6F), −57.36 (m, 6F). HR MS (FAB, positive, *m*-NBA): calcd for $C_{38}H_{20}F_{12}IrN_4$ ($[M-PF_6]^+$), 953.1126; found, 953.1128. Anal. Calcd for $C_{38}H_{20}F_{18}IrN_4P$: C, 41.58; H, 1.84; N, 5.10. Found: C, 41.81; H, 1.88; N, 4.97.

ZIrfppy. The synthesis method described above was applied to $[(fppy)_2Ir(\mu\text{-}Cl)]_2$ (0.221 g, 0.193 mmol) and 4-(di(2-picolyl)-aminomethyl)-1,10-phenanthroline (0.128 g, 0.328 mmol) to give a yellow solid (0.178 g, 0.159 mmol) in an 82% yield. ^{1}H NMR ($CDCl_3$, 400 MHz): δ 3.94 (s, 4H), 4.47 (dd, J = 5.3, 1.6 Hz, 2H), 5.98 (m, 2H), 6.82 (m, 2H), 6.88 (m, 1H), 6.96 (m, 1H), 7.13 (dd, J = 7.5, 4.9 Hz, 2H), 7.23 (m, 1H), 7.31 (m, 1H), 7.47 (d, J = 7.9 Hz, 2H), 7.65 (m, 2H), 7.73 (m, 4H), 7.83 (m, 3H), 8.10 (d, J = 5.2 Hz, 1H), 8.16 (d, J = 5.2 Hz, 1H), 8.21 (d, J = 9.2 Hz, 1H), 8.24 (dd, J = 5.0, 1.4 Hz, 1H), 8.38 (d, J = 9.2 Hz, 1H), 8.50 (d, J = 4.9 Hz, 2H), 8.68 (dd, J = 8.3, 1.4 Hz, 1H). ^{13}C NMR (CD_3CN, 100 MHz): δ 109.69, 119.99, 123.39, 126.83, 127.04, 127.13, 128.32, 131.67, 138.80, 140.79, 146.70, 149.38, 151.49, 152.76, 152.81, 162.44, 164.95, 166.31. ^{19}F NMR ($CDCl_3$, 376 MHz): δ −108.43 (m, 1F), −108.17 (m, 1F), −73.48 (d, J = 711 Hz, 6F). HR MS (FAB, positive, *m*-NBA): calcd for $C_{47}H_{35}F_4IrN_7$ ($[M-PF_6]^+$), 930.2708; found, 930.2711. Anal. Calcd for $C_{47}H_{35}F_{10}IrN_7P$: C, 52.51; H, 3.47; N, 9.12. Found: C, 52.64; H, 3.44; N, 8.98.

Irfppy. The synthesis method described above was applied to $[(fppy)_2Ir(\mu\text{-}Cl)]_2$ (0.747 g, 0.653 mmol) and 1,10-phenanthroline (0.200 g, 1.11 mmol) to afford a yellow solid (0.215 g, 0.238 mmol) in a 36% yield. ^{1}H NMR (CD_3CN, 400 MHz): δ 5.99 (dd, J = 9.2, 2.6 Hz, 2H), 6.84−6.90 (m, 4H), 7.37 (d, J = 5.8 Hz, 2H), 7.80 (m, 2H), 7.84−7.91 (m, 4H), 8.01 (d, J = 8.1 Hz, 2H), 8.24 (s, 2H), 8.33 (dd, J = 5.0, 1.4 Hz, 2H), 8.70 (dd, J = 8.2, 1.4 Hz, 2H). ^{13}C NMR (CD_3CN, 100 MHz): δ 55.15, 60.66, 109.64, 119.98, 122.25, 123.29, 123.41, 125.23, 126.69, 126.76, 127.03, 127.12, 127.50, 136.37, 138.54, 138.74, 148.95, 149.14, 149.34, 150.80, 151.42, 158.60. ^{19}F NMR (CD_3CN, 376 MHz): δ −111.14 (m, 2F), −72.97 (d, J = 707 Hz, 6F). Anal. Calcd for $C_{34}H_{22}F_8IrN_4P$: C, 47.39; H, 2.57; N, 6.50. Found: C, 47.31; H, 2.70; N, 6.57.

ZIrpbt. The synthesis method described above was applied to $[(pbt)_2Ir(\mu\text{-}Cl)]_2$ (0.620 g, 0.478 mmol) and 4-(di(2-picolyl)-aminomethyl)-1,10-phenanthroline (0.319 g, 0.820 mmol) to yield an orange solid (0.382 g, 0.332 mmol) in a 70% yield. ^{1}H NMR ($CDCl_3$, 400 MHz): δ 3.92 (dd, J = 2.9, 1.4 Hz, 4H), 4.43 (dd, J = 4.3, 1.5 Hz, 2H), 5.62 (d, J = 8.4 Hz, 1H), 5.82 (d, J = 8.4 Hz, 1H), 6.46 (t, J = 7.3 Hz, 2H), 6.52 (m, 1H), 6.89−6.97 (m, 3H), 7.06 (m, 2H), 7.10−7.16 (m, 3H), 7.38 (d, J = 7.8 Hz, 2H), 7.60 (td, J = 7.6, 1.8 Hz, 2H), 7.74 (d, J = 7.6 Hz, 1H), 7.79 (d, J = 7.6 Hz, 1H), 7.85 (m, 2H), 7.91 (dd, J = 8.2, 5.1 Hz, 1H), 8.05 (d, J = 5.3 Hz, 1H), 8.23−8.30 (m, 3H), 8.37 (dd, J = 5.0, 1,4 Hz, 1H), 8.49 (m, 2H), 8.83 (dd, J = 8.3, 1.4 Hz, 1H). ^{13}C NMR (CD_3CN, 100 MHz): δ 55.10, 60.66, 117.07, 117.58, 122.78, 123.55, 123.98, 125.21, 126.03, 126.25, 126.94, 127.01, 127.16, 127.87, 128.40, 128.82, 130.77, 131.32, 131.40, 132.49, 133.73, 133.82, 137.17, 139.88, 140.40, 147.80, 147.90, 149.17, 149.32, 149.47, 149.79, 149.93, 150.04, 150.65, 151.14, 157.91, 181.51. HR MS (FAB, positive, *m*-NBA): calcd for $C_{51}H_{37}IrN_7S_2$ ($[M-PF_6]^+$), 1004.2181; found, 1004.2314. Anal. Calcd for $C_{51}H_{37}F_6IrN_7S_2P$: C, 53.30; H, 3.25; N, 8.53; S, 5.58. Found: C, 52.91; H, 3.35; N, 8.18; S, 5.56.

Irpbt. The synthesis method described above was applied to $[(pbt)_2Ir(\mu\text{-}Cl)]_2$ (0.200 g, 0.154 mmol) and 1,10-phenanthroline (0.0472 g, 0.262 mmol) to afford a yellow solid (0.136 g, 0.145 mmol) in a 94% yield. ^{1}H NMR (CD_3CN, 400 MHz): δ 5.83 (m, 2H), 6.51 (m, 2H), 6.84−6.89 (m, 2H), 6.94 (td, J = 7.6, 1.4 Hz, 2H), 7.16 (td, J = 7.6, 1.1 Hz, 2H), 7.25 (m, 2H), 7.89−7.98 (m, 6H), 8.47 (dd, J = 5.1, 1.4, 2H), 8.70 (dd, J = 8.3, 1.4 Hz, 2H). ^{13}C NMR (CD_3CN, 100 MHz): δ 111.38, 124.42, 124.88, 126.98, 127.86, 128.14, 128.83, 129.32, 132.21, 132.65, 132.96, 134.53, 140.14, 141.74, 148.62, 150.23, 150.82, 152.87. HR MS (FAB, positive, *m*-NBA): calcd for $C_{38}H_{24}IrN_4S_2$ ($[M-PF_6]^+$), 793.1072; found, 793.1071. Anal. Calcd for $C_{38}H_{24}F_6IrN_4S_2P$: C, 48.66; H, 2.58; N, 5.97; S, 6.84. Found: C, 48.72; H, 2.75; N, 6.19; S, 6.75.

ZIrppy. The synthesis method described above was applied to $[(ppy)_2Ir(\mu\text{-}Cl)]_2$ (0.323 g, 0.301 mmol) and 4-(di(2-picolyl)-aminomethyl)-1,10-phenanthroline (0.200 g, 0.512 mmol) to give a yellow solid (0.272 g, 0.262 mmol) in an 87% yield. ^{1}H NMR ($CDCl_3$, 400 MHz): δ 3.95 (s, 4H), 4.45 (dd, J = 5.0, 1.6 Hz, 2H), 6.36 (m, 2H), 6.85 (m, 1H), 6.92−6.98 (m, 3H), 7.07 (m, 2H), 7.12 (m, 2H), 7.28 (m, 1H), 7.36 (m, 1H), 7.47 (d, J = 7.8 Hz, 2H), 7.68 (m, 2H), 7.67−7.72 (m, 4H), 7.77 (dd, J = 8.2, 5.0 Hz, 1H), 7.90 (t, J = 8.3 Hz, 2H), 8.03 (d, J = 5.3 Hz, 1H), 8.15 (d, J = 5.2 Hz, 1H), 8.19 (d, J = 9.2 Hz, 1H), 8.23 (dd, J = 5.0, 1.4 Hz, 1H), 8.36 (d, J = 9.2 Hz, 1H), 8.50 (m, 2H), 8.65 (dd, J = 8.3, 1.4 Hz, 1H). ^{13}C NMR ($CDCl_3$, 100 MHz): δ 50.63, 53.62, 55.18, 60.82, 119.77, 122.75, 122.79, 123.41, 123.50, 123.91, 124.90, 126.58, 128.46, 130.75, 130.83, 131.32, 131.89, 131.94, 137.20, 138.33, 138.86, 143.83, 146.70, 148.54, 148.75, 149.10, 149.23, 149.85, 149.92, 150.45, 150.92, 157.96, 167.83, 167.88. HR MS (FAB, positive, *m*-NBA): calcd for $C_{47}H_{37}IrN_7$ ($[M-PF_6]^+$), 892.2740; found, 892.2743. Anal. Calcd for $C_{47}H_{37}F_6IrN_7P$: C, 54.43; H, 3.60; N, 9.45. Found: C, 54.25; H, 3.54; N, 9.05.

Irppy. The synthesis method described above was applied to $[(ppy)_2Ir(\mu\text{-}Cl)]_2$ (0.300 g, 0.280 mmol) and 1,10-phenanthroline (0.0870 g, 0.480 mmol) to afford a yellow solid (33 mg, 40 μmol) in a 14% yield. ^{1}H NMR (CD_3CN, 400 MHz): δ 6.39 (dd, J = 7.6, 0.8 Hz, 2H), 6.86 (m, 2H), 6.96 (td, J = 7.4, 1.4 Hz, 2H), 7.07 (td, J = 7.3, 1.2 Hz, 2H), 7.42 (d, J = 5.8 Hz, 2H), 7.77 (m, 2H), 7.84 (m, 4H), 8.05 (m, 2H), 8.23 (s, 2H), 8.30 (dd, J = 5.1, 1.4 Hz, 2H), 8.68 (dd, J = 8.3, 1.4 Hz, 2H). ^{13}C NMR (CD_3CN, 100 MHz): δ 118.38, 120.84, 123.68, 124.42, 125.92, 131.39, 132.68, 132.79, 139.51, 139.58, 145.39, 147.90, 150.45, 150.87, 152.29, 168.54. HR MS (FAB, positive, *m*-NBA): calcd for $C_{34}H_{24}IrN_4$ ($[M-PF_6]^+$), 681.1630; found, 681.1631. Anal. Calcd for $C_{34}H_{24}F_6IrN_4P$: C, 49.45; H, 2.93; N, 6.78. Found: C, 49.35; H, 3.06; N, 6.71.

ZIrbtp. The synthesis method described above was applied to $[(btp)_2Ir(\mu\text{-}Cl)]_2$ (0.389 g, 0.300 mmol) and 4-(di(2-picolyl)-aminomethyl)-1,10-phenanthroline (0.200 g, 0.512 mmol) to give an orange solid (0.147 g, 0.128 mmol) in a 43% yield. ^{1}H NMR ($CDCl_3$, 400 MHz): δ 3.95 (s, 4H), 4.48 (dd, J = 5.3, 1.6 Hz, 2H), 6.06 (t, J = 8.0 Hz, 2H), 6.74 (m, 1H), 6.84 (m, 1H), 6.89 (m, 2H), 7.14 (m, 2H), 7.22 (m, 3H), 7.31 (m, 1H), 7.45 (d, J = 7.8 Hz, 2H), 7.62−7.74 (m, 6H), 7.82 (m, 2H), 8.08 (dd, J = 5.3, 2.0 Hz, 2H), 8.19−8.24 (m, 2H), 8.38 (d, J = 9.2 Hz, 1H), 8.51 (d, J = 4.1 Hz, 2H), 8.68 (dd, J = 8.3, 1.4 Hz, 1H). ^{13}C NMR ($CDCl_3$, 100 MHz): δ 53.65, 54.93, 60.76, 119.80, 121.33, 121.40, 122.68, 123.26, 123.86, 124.68, 125.09, 125.36, 125.97, 126.64, 126.84, 128.67, 130.98, 131.51, 136.74, 137.02, 139.55, 139.66, 142.97, 145.57, 146.79, 147.84, 147.95, 149.27, 149.40, 149.69, 150.53, 151.07, 151.48, 158.02, 164.81, 164.86. HR MS (FAB, positive, *m*-NBA): calcd for $C_{51}H_{37}IrN_7S_2$ ($[M-PF_6]^+$), 1004.2181; found, 1004.2182. Anal. Calcd for $C_{51}H_{37}F_6IrN_7PS_2$: C, 53.30; H, 3.25; N, 8.53; S, 5.58. Found: C, 53.06; H, 3.38; N, 8.15; S, 5.48.

Irbtp. The synthesis method described above was applied to $[(btp)_2Ir(\mu\text{-}Cl)]_2$ (0.120 g, 0.154 mmol) and 1,10-phenanthroline (0.0473 g, 0.262 mmol) to afford an orange solid (0.033 g, 0.0352 mmol) in a 23% yield. ^{1}H NMR (MeOD, 400 MHz): δ 6.14 (d, J = 8.0 Hz, 2H), 6.78−6.86 (m, 4H), 7.17 (td, J = 8.2, 1.1 Hz, 2H), 7.43 (m, 2H), 7.77−7.87 (m, 8H), 8.28 (m, 4H), 8.73 (dd, J = 7.5, 1.4 Hz, 2H). ^{13}C NMR (CD_3CN, 100 MHz): δ 119.58, 121.29, 123.24, 124.40, 125.86, 127.16, 128.40, 139.10, 139.86, 150.37, 152.13. HR MS (FAB, positive, *m*-NBA): calcd for $C_{38}H_{24}IrN_4S_2$ ($[M-PF_6]^+$), 793.1072; found, 793.1081.

ZIrOMe. The synthesis method described above was applied to $[(OMe)_2Ir(\mu\text{-}Cl)]_2$ (0.250 g, 0.209 mmol) and 4-(di(2-picolyl)-aminomethyl)-1,10-phenanthroline (0.138 g, 0.354 mmol) to give a reddish orange solid (0.193 g, 0.170 mmol) in an 81% yield. ^{1}H NMR ($CDCl_3$, 400 MHz): δ 3.82 (d, J = 4.7 Hz, 6H), 3.94 (s, 4H), 4.44 (dd, J = 5.0, 1.6 Hz, 2H), 6.24 (dd, J = 8.3, 5.2 Hz, 2H), 6.68 (m, 2H), 6.84 (m, 1H), 6.93 (m, 1H), 7.13 (m, 2H), 7.28 (m, 3H), 7.35 (m, 1H), 7.47 (d, J = 7.8 Hz, 2H), 7.63−7.69 (m, 4H), 7.78 (dd, J = 8.2, 5.0 Hz, 1H), 7.85 (t, J = 8.3 Hz, 2H), 8.03 (d, J = 5.3 Hz, 1H), 8.18 (m, 2H), 8.26 (dd, J = 5.0, 1.4 Hz, 1H), 8.36 (d, J = 9.2 Hz, 1H), 8.50 (m, 2H), 8.64 (dd, J = 8.3, 1.4 Hz, 1H). ^{13}C NMR ($CDCl_3$, 100 MHz): δ 55.36, 60.80, 110.19, 117.76, 119.86, 122.55, 123.51, 123.71, 124.81, 126.61,

dx.doi.org/10.1021/ja3123202 | J. Am. Chem. Soc. 2013, 135, 4771−4787

128.30, 130.63, 131.16, 132.05, 132.10, 136.88, 138.22, 139.22, 139.32, 144.07, 146.89, 148.52, 148.71, 149.12, 149.17, 150.44, 150.91, 156.25, 158.00, 167.56, 167.61. HR MS (FAB, positive, *m*-NBA): calcd for $C_{49}H_{41}IrN_7O_2$ ($[M-PF_6]^+$) 952.2951; found, 952.2954. Anal. Calcd for $C_{49}H_{41}F_6IrN_7O_2P$: C, 53.64; H, 3.77; N, 8.94. Found: C, 53.47; H, 3.77; N, 8.68.

IrOMe. The synthesis method described above was applied to $[(OMe)_2Ir(\mu\text{-}Cl)]_2$ (0.320 g, 0.268 mmol) and 1,10-phenanthroline (0.0822 g, 0.456 mmol) to afford a reddish orange solid (0.193 g, 0.170 mmol) in an 81% yield. ^{1}H NMR ($CDCl_3$, 400 MHz): δ 3.83 (s, 6H), 6.28 (d, J = 8.3 Hz, 2H), 6.70 (dd, J = 8.3, 2.6 Hz, 2H), 6.90 (m, 2H), 7.30 (d, J = 2.6 Hz, 2H), 7.35 (m, 2H), 7.69 (td, J = 8.1, 1.5 Hz, 2H), 7.84 (m, 4H), 8.21 (s, 2H), 8.30 (dd, J = 5.0, 1.4 Hz, 2H), 8.64 (dd, J = 8.2, 1.4 Hz, 2H). ^{13}C NMR ($CDCl_3$, 100 MHz): δ 55.59, 110.60, 117.86, 119.90, 123.69, 126.80, 131.77, 132.35, 138.28, 139.03, 139.11, 144.19, 147.04, 148.96, 151.06, 156.53, 167.84. Anal. calcd for $C_{36}H_{28}F_6IrN_4O_2P$: C, 48.81; H, 3.19; N, 6.32. Found: C, 48.77; H, 3.28; N, 6.27.

Spectroscopic Measurements. Milli-Q grade water (18.2 MΩ·cm) and spectrophotometric grade CH_3CN (Aldrich) were used to prepare solutions for the spectroscopic measurements. HEPES (4-(2-hydroxyethyl)-1-piperazineethanesulfonic acid, ≥99%) was purchased from Aldrich. An aqueous pH 7.4 buffer solution was prepared by dissolving HEPES (50 mM) and Puratronic grade KCl (100 mM, CalBiochem) in milli-Q water and adjusting the pH using a standard KOH solution (45 wt %, Aldrich) or an HCl solution (1 N, Aldrich). The buffer solution was further treated with Chelex100 resin (BIO-RAD) to remove trace metal ions and filtered through a membrane (pore size = 0.45 μm). The pH of the buffer solution was reexamined prior to use. Fresh metal stock solutions (typically, 0.1 or 0.01 M) were prepared in milli-Q water using the corresponding chloride salts: NaCl (≥99.5%, Aldrich), $MgCl_2$ (99.99%, Aldrich), $CaCl_2$ (99.99%, Aldrich), $CrCl_2$ (99.99%, Aldrich), $MnCl_2$ (99.99%, Aldrich), $FeCl_2$ (99.99%, Aldrich), $CoCl_2$ (99.9%, Aldrich), $NiCl_2$ (99.99%, Aldrich), $ZnCl_2$ (99.999%, Aldrich), and $CuCl_2$ (99.999%, Aldrich). A TPEN solution was prepared by dissolving *N*,*N*,*N*′,*N*′-tetrakis(2-picolyl)ethylenediamine (≥99%, Sigma) in DMSO (99.9%, Aldrich). $Zn(ClO_4)_2\cdot 6H_2O$ (Aldrich) was dissolved in CH_3CN (spectrophotometric grade, Aldrich) to 1 mM, 10 mM, and 100 mM concentration. The Ir(III) complex solutions were prepared by dissolution in CH_3CN to concentrations of 10 mM, 1 mM, 100 μM, and 10 μM. The 10 μM solutions were used for spectroscopic measurements. For aqueous solutions, 3 mL of the HEPES buffer containing 5 vol % DMSO and 3 μL of the Ir(III) complex solution (10 mM in DMSO) were mixed to give a 10 μM solution. A 1 cm × 1 cm fluorimeter cell (Hellma) was used for the steady-state optical measurements. UV−vis absorption spectra were collected on a Varian Cary 50 spectrophotometer at room temperature. Phosphorescence spectra were obtained using a Quanta Master 40 scanning spectrofluorimeter at room temperature. The solutions were excited at the following wavelengths: 393 (ZIrdCF3), 359 (ZIrdfppy), 362 (ZIrfppy), 412 (ZIrpbt), 377 (ZIrppy), 434 (ZIrbtp), and 377 nm (ZIrOMe) throughout phosphorescence measurements. The phosphorescence quantum yields were relatively determined according to the following standard equation: $\Phi = \Phi_{ref}(I/I_{ref})(A_{ref}/A)(n/n_{ref})^2$, where A, I, and n are the absorbance at the excitation wavelength, integrated photoluminescence intensity, and the refractive index of the solvent, respectively. Fluorescein as an aqueous 0.1 N NaOH solution was used as the external reference (Φ_{ref} = 0.79). The refractive index of the 0.1 N NaOH solution was assumed to be identical to the value for pure water. The 10 μM solutions were thoroughly degassed through the repeated vacuum−freeze−thaw cycles prior to performing the measurements. Ar-saturated 50 μM solutions (CH_3CN) were used in determining the phosphorescence lifetimes. Phosphorescence decay traces were acquired based on TCSPC techniques using a FluoTime 200 instrument (PicoQuant, Germany). A 377 nm diode laser (PicoQuant, Germany) was used as the excitation source. The phosphorescence signals were obtained using an automated motorized monochromator. Phosphorescence decay profiles were analyzed (OriginPro 8.0, OriginLab) using a single exponential decay model. The measurements were performed in duplicate using fresh samples in the absence or presence of zinc ions (2 equiv).

Electrochemical Measurements. Cyclic voltammetry (CV) and differential pulse voltammetry (DPV) experiments were carried out using a CHI630B instrument (CH Instruments, Inc.) using three-electrode cell assemblies. A Pt wire and a Pt disc were used as the counter and working electrodes, respectively. A $Ag/AgNO_3$ couple was used as a pseudo reference electrode. Measurements were carried out in Ar-saturated CH_3CN (3 mL) using tetra-*n*-butylammonium hexafluorophosphate (Bu_4NPF_6) as the supporting electrolyte (0.10 M) at scan rates of 100 mV/s (CV) and 4 mV/s (DPV). The concentration of the Ir(III) complex was 1.0 mM. A ferrocenium/ferrocene reference was employed as the external reference.

Calculations. Quantum chemical calculations based on DFT were carried out using Gaussian 09.[107] An *N*,*N*-trans structure was employed as the starting geometry. Ground-state geometry optimization and single-point calculations were performed using Becke's three-parameter B3LYP exchange-correlation functional,[108−110] the "double-ξ" quality LANL2DZ basis set for the Ir atom, and the 6-31+G(d,p) basis set for all other atoms. A pseudo potential (LANL2DZ) was applied to replace the inner core electrons of the Ir atom, leaving the outer core $[(5s)^2(5p)^6]$ electrons and the $(5d)^6$ valence electrons. The polarizable continuum model (C-PCM), parametrized for acetonitrile solvent, was applied during the geometry optimization step. Frequency calculations were subsequently performed to assess the stability of the convergence. For TD-DFT calculations, the unrestricted B3LYP functional and basis sets identical to those used for the geometry optimization were applied. C-PCM, parametrized for acetonitrile solvent, was applied to account for solvation effects. The 20 lowest triplet and singlet states were calculated and analyzed.

Cell Culture. HeLa cells purchased from Korean Cell Line Bank were cultured in DMEM supplemented with 10% fetal bovine serum and penicillin (100 units/mL) at 37 °C in a humidified incubator under 5% CO_2.

Confocal Laser Scanning Microscopy. One day prior to imaging, HeLa cells were plated onto glass-bottom culture dishes. After 24 h, the cells were washed and supplemented with fresh DMEM. The cells were treated with 50 μM TPEN for 5 min at 37 °C and washed with 2 mL serum-free DMEM. A 10 μM ZIrdCF3 aliquot was added to the DMEM, and the cells were incubated for 10 min at 37 °C. The cells were washed twice with fresh DMEM to remove the remaining probe. The cells were imaged by confocal laser-scanning microscopy in the absence and presence of 200 μM $ZnCl_2$/NaPT. A Carl Zeiss LSM 510 META confocal laser scanning microscope was used to obtain phosphorescence images. An excitation beam (405 nm) was focused onto the dish, and the signals were acquired through 30 emission channels covering the range 410−691 nm. Phosphorescence images and mean intensities were analyzed using the LSM 510 version 4.0 software.

Photoluminescence Lifetime Imaging Microscopy. The medium was removed from the culture dish, and the cells were rinsed with PBS. The cells were fixed using 4% formaldehyde, and subsequently mounted with Vectashield (Vector Labs). An inverse time-resolved microscope (PicoQuant, MicroTime 200) was employed for the photoluminescence experiments. A 375 nm picosecond pulsed diode laser (<1 μW) operated at a 2.5 MHz repetition rate was used for excitation. The instrumental response function of the system was ~240 ps at fwhm. A dichroic mirror (Z375RDC, AHF), a long-pass filter (HQ405lp, AHF), a 50 μm pinhole, a 550 nm band-pass filter (FB550-40, Thorlabs), and a single photon avalanche diode were used to collect emission from the HeLa cells. The time-resolved emission signals were obtained using a TCSPC technique. Typically, an 80 μm × 80 μm sample area consisting of 200 × 200 pixels was scanned with an acquisition rate of 2 ms/pixel. Photoluminescence lifetime images and their exponential fits were analyzed using the SymPhoTime software provided by the manufacturer.

dx.doi.org/10.1021/ja3123202 | J. Am. Chem. Soc. 2013, 135, 4771−4787

■ ASSOCIATED CONTENT

Supporting Information

Figures S1−S43, displaying the ^{1}H, ^{13}C, and ^{19}F NMR spectra, UV−vis absorption spectra, phosphorescence response to other Lewis acids in acetonitrile, cyclic and differential pulse voltammograms, phosphorescence decay traces, phosphorescence zinc response in HEPES buffers, concentration dependence of the phosphorescence spectra, a limit of zinc detection value, phosphorescent zinc titration, Job's plot, phosphorescence decay traces in HEPES buffers, MTT cell viability data, and gel electrophoretic analysis of pUC19 plasmid DNA treated with ZIrdCF3. This material is available free of charge via the Internet at http://pubs.acs.org.

■ AUTHOR INFORMATION

Corresponding Author

odds2@khu.ac.kr (Y.Y.); wwnam@ewha.ac.kr (W.N.)

Present Address

[‡]Y.Y.: Department of Advanced Materials Engineering for Information and Electronics, Kyung Hee University, Yongin-si 446-701, Korea

Author Contributions

[†]H.W. and S.C. contributed equally to this work.

Notes

The authors declare no competing financial interest.

■ ACKNOWLEDGMENTS

This work was supported by the CRI (W.N.), GRL (2010-00353) (W.N.), WCU (R31-2008-000-10010-0) (W.N.), and BSR programs (2012-0001408) (W.C.) (2011-0009172) (D.-R.A.) from the National Research Foundation (NRF) of Korea, and RP-Grant 2010 (Y.Y.) from the Ewha Womans University.

■ REFERENCES

(1) Grynkiewicz, G.; Poenie, M.; Tsien, R. Y. *J. Biol. Chem.* **1985**, *260*, 3440−3450.
(2) Tsien, R. Y. *Biochemistry* **1980**, *19*, 2396−2404.
(3) Que, E. L.; Domaille, D. W.; Chang, C. J. *Chem. Rev.* **2008**, *108*, 1517−1549.
(4) Chan, J.; Dodani, S. C.; Chang, C. J. *Nat. Chem.* **2012**, *4*, 973−984.
(5) Domaille, D. W.; Que, E. L.; Chang, C. J. *Nat. Chem. Biol.* **2008**, *4*, 168−175.
(6) Bertini, I.; Gray, H. B.; Steifel, E.; Valentine, J. S. *Biological Inorganic Chemistry*; University Science Books: Sausalito, CA, 2007.
(7) Lippard, S. J.; Berg, J. M. *Principles of Bioinorganic Chemistry*; University Science Books: Mill Valley, CA, 1994.
(8) Nolan, E. M.; Lippard, S. J. *Acc. Chem. Res.* **2009**, *42*, 193−203.
(9) Lim, N. C.; Freake, H. C.; Brueckner, C. *Chem.—Eur. J.* **2005**, *11*, 38−49.
(10) Kimura, E.; Koike, T. *Chem. Soc. Rev.* **1998**, *27*, 179−184.
(11) Xu, Z.; Yoon, J.; Spring, D. R. *Chem. Soc. Rev.* **2010**, *39*, 1996−2006.
(12) Jiang, P.; Guo, Z. *Coord. Chem. Rev.* **2004**, *248*, 205−229.
(13) Tomat, E.; Lippard, S. J. *Curr. Opin. Chem. Biol.* **2010**, *14*, 225−230.
(14) Frederickson, C. J.; Kasarskis, E. J.; Ringo, D.; Frederickson, R. E. *J. Neurosci. Methods* **1987**, *20*, 91−103.
(15) Linert, W.; Jameson, G. N. L.; Jameson, R. F.; Jellinger, K. A. *Met. Ions Life Sci.* **2006**, *1*, 281−320.
(16) Dai, Z.; Canary, J. W. *New J. Chem.* **2007**, *31*, 1708−1718.
(17) Qian, F.; Zhang, C.; Zhang, Y.; He, W.; Gao, X.; Hu, P.; Guo, Z. *J. Am. Chem. Soc.* **2009**, *131*, 1460−1468.
(18) Hanaoka, K.; Muramatsu, Y.; Urano, Y.; Terai, T.; Nagano, T. *Chem.—Eur. J.* **2010**, *16*, 568−572.
(19) Aoki, S.; Kagata, D.; Shiro, M.; Takeda, K.; Kimura, E. *J. Am. Chem. Soc.* **2004**, *126*, 13377−13390.
(20) Henary, M. M.; Wu, Y.; Fahrni, C. J. *Chem.—Eur. J.* **2004**, *10*, 3015−3025.
(21) Taki, M.; Wolford, J. L.; O'Halloran, T. V. *J. Am. Chem. Soc.* **2004**, *126*, 712−713.
(22) Fahrni, C. J.; Henary, M. M.; VanDerveer, D. G. *J. Phys. Chem. A* **2002**, *106*, 7655−7663.
(23) Henary, M. M.; Fahrni, C. J. *J. Phys. Chem. A* **2002**, *106*, 5210−5220.
(24) Kwon, J. E.; Lee, S.; You, Y.; Baek, K.-H.; Ohkubo, K.; Cho, J.; Fukuzumi, S.; Shin, I.; Park, S. Y.; Nam, W. *Inorg. Chem.* **2012**, *51*, 8760−8774.
(25) Ueno, T.; Urano, Y.; Setsukinai, K.-i.; Takakusa, H.; Kojima, H.; Kikuchi, K.; Ohkubo, K.; Fukuzumi, S.; Nagano, T. *J. Am. Chem. Soc.* **2004**, *126*, 14079−14085.
(26) Fahrni, C. J.; Yang, L.; VanDerveer, D. G. *J. Am. Chem. Soc.* **2003**, *125*, 3799−3812.
(27) Hirano, T.; Kikichi, K.; Urano, Y.; Higuchi, T.; Nagano, T. *Angew. Chem., Int. Ed.* **2000**, *39*, 1052−1054.
(28) Gee, K. R.; Zhou, Z.-L.; Ton-That, D.; Sensi, S. L.; Weiss, J. H. *Cell Calcium* **2002**, *31*, 245−251.
(29) Aoki, S.; Sakurama, K.; Matsuo, N.; Yamada, Y.; Takasawa, R.; Tanuma, S.-i.; Shiro, M.; Takeda, K.; Kimura, E. *Chem.—Eur. J.* **2006**, *12*, 9066−9080.
(30) Burdette, S. C.; Walkup, G. K.; Spingler, B.; Tsien, R. Y.; Lippard, S. J. *J. Am. Chem. Soc.* **2001**, *123*, 7831−7841.
(31) Gee, K. R.; Zhou, Z.-L.; Qian, W.-J.; Kennedy, R. *J. Am. Chem. Soc.* **2002**, *124*, 776−778.
(32) Koike, T.; Watanabe, T.; Aoki, S.; Kimura, E.; Shiro, M. *J. Am. Chem. Soc.* **1996**, *118*, 12696−12703.
(33) Nolan, E. M.; Jaworski, J.; Okamoto, K.; Hayashi, Y.; Sheng, M.; Lippard, S. J. *J. Am. Chem. Soc.* **2005**, *127*, 16812−16823.
(34) Gunnlaugsson, T.; Lee, T. C.; Parkesh, R. *Org. Biomol. Chem.* **2003**, *1*, 3265−3267.
(35) Weller, A. *Pure. Appl. Chem.* **1968**, *16*, 115−123.
(36) de Silva, A. P.; Moody, T. S.; Wright, G. D. *Analyst* **2009**, *134*, 2385−2393.
(37) de Silva, A. P.; Gunaratne, H. Q. N.; Gunnlaugsson, T.; Huxley, A. J. M.; McCoy, C. P.; Rademacher, J. T.; Rice, T. E. *Chem. Rev.* **1997**, *97*, 1515−1566.
(38) Kavarnos, G. J.; Turro, N. J. *Chem. Rev.* **1986**, *86*, 401−449.
(39) Chang, C. J.; Nolan, E. M.; Jaworski, J.; Burdette, S. C.; Sheng, M.; Lippard, S. J. *Chem. Biol.* **2004**, *11*, 203−210.
(40) Chang, C. J.; Nolan, E. M.; Jaworski, J.; Okamoto, K.; Hayashi, Y.; Sheng, M.; Lippard, S. J. *Inorg. Chem.* **2004**, *43*, 6774−6779.
(41) Nolan, E. M.; Burdette, S. C.; Harvey, J. H.; Hilderbrand, S. A.; Lippard, S. J. *Inorg. Chem.* **2004**, *43*, 2624−2635.
(42) Burdette, S. C.; Frederickson, C. J.; Bu, W.; Lippard, S. J. *J. Am. Chem. Soc.* **2003**, *125*, 1778−1787.
(43) Hirano, T.; Kikuchi, K.; Urano, Y.; Nagano, T. *J. Am. Chem. Soc.* **2002**, *124*, 6555−6562.
(44) Sun, W.-C.; Gee, K. R.; Klaubert, D. H.; Haugland, R. P. *J. Org. Chem.* **1997**, *62*, 6469−6475.
(45) Leonhardt, H.; Gordon, L.; Livingston, R. *J. Phys. Chem.* **1971**, *75*, 245−249.
(46) Goldsmith, C. R.; Lippard, S. J. *Inorg. Chem.* **2006**, *45*, 555−561.
(47) Nolan, E. M.; Jaworski, J.; Racine, M. E.; Sheng, M.; Lippard, S. J. *Inorg. Chem.* **2006**, *45*, 9748−9757.
(48) Nolan, E. M.; Lippard, S. J. *Inorg. Chem.* **2004**, *43*, 8310−8317.
(49) Komatsu, K.; Kikuchi, K.; Kojima, H.; Urano, Y.; Nagano, T. *J. Am. Chem. Soc.* **2005**, *127*, 10197−10204.
(50) Nolan, E. M.; Ryu, J. W.; Jaworski, J.; Feazell, R. P.; Sheng, M.; Lippard, S. J. *J. Am. Chem. Soc.* **2006**, *128*, 15517−15528.
(51) Sunahara, H.; Urano, Y.; Kojima, H.; Nagano, T. *J. Am. Chem. Soc.* **2007**, *129*, 5597−5604.

(52) Lu, H.; Zhang, S.; Liu, H.; Wang, Y.; Shen, Z.; Liu, C.; You, X. *J. Phys. Chem. A* **2009**, *113*, 14081−14086.
(53) Koide, Y.; Urano, Y.; Hanaoka, K.; Terai, T.; Nagano, T. *ACS Chem. Biol.* **2011**, *6*, 600−608.
(54) McCarroll, M. E.; Shi, Y.; Harris, S.; Puli, S.; Kimaru, I.; Xu, R.; Wang, L.; Dyer, D. J. *J. Phys. Chem. B* **2006**, *110*, 22991−22994.
(55) Montgomery, C. P.; Murray, B. S.; New, E. J.; Pal, R.; Parker, D. *Acc. Chem. Res.* **2009**, *42*, 925−937.
(56) Song, C.; Ye, Z.; Wang, G.; Yuan, J.; Guan, Y. *Chem.—Eur. J.* **2010**, *16*, 6464−6472.
(57) Hanaoka, K.; Kikuchi, K.; Kobayashi, S.; Nagano, T. *J. Am. Chem. Soc.* **2007**, *129*, 13502−13509.
(58) Marti, A. A.; Puckett, C. A.; Dyer, J.; Stevens, N.; Jockusch, S.; Ju, J.; Barton, J. K.; Turro, N. J. *J. Am. Chem. Soc.* **2007**, *129*, 8680−8681.
(59) Song, B.; Wang, G.; Tan, M.; Yuan, J. *J. Am. Chem. Soc.* **2006**, *128*, 13442−13450.
(60) Wu, J.; Ye, Z.; Wang, G.; Jin, D.; Yuan, J.; Guan, Y.; Piper, J. *J. Mater. Chem.* **2009**, *19*, 1258−1264.
(61) You, Y.; Lee, S.; Kim, T.; Ohkubo, K.; Chae, W.-S.; Fukuzumi, S.; Jhon, G.-J.; Nam, W.; Lippard, S. J. *J. Am. Chem. Soc.* **2011**, *133*, 18328−18342.
(62) Lee, P.-K.; Law, W. H.-T.; Liu, H.-W.; Lo, K. K.-W. *Inorg. Chem.* **2011**, *50*, 8570−8579.
(63) Hanss, D.; Freys, J. C.; Bernardinelli, G.; Wenger, O. S. *Eur. J. Inorg. Chem.* **2009**, 4850−4859.
(64) Li, J.; Djurovich, P. I.; Alleyne, B. D.; Yousufuddin, M.; Ho, N. N.; Thomas, J. C.; Peters, J. C.; Bau, R.; Thompson, M. E. *Inorg. Chem.* **2005**, *44*, 1713−1727.
(65) Lowry, M. S.; Bernhard, S. *Chem.—Eur. J.* **2006**, *12*, 7970−7977.
(66) Dixon, I. M.; Collin, J.-P.; Sauvage, J.-P.; Flamigni, L.; Encinas, S.; Barigelletti, F. *Chem. Soc. Rev.* **2000**, *29*, 385−391.
(67) You, Y.; Park, S. Y. *Dalton Trans.* **2009**, 1267−1282.
(68) Baranoff, E.; Yum, J.-H.; Grätzel, M.; Nazeeruddin, M. K. *J. Organomet. Chem.* **2009**, *694*, 2661−2670.
(69) Lo, K. K.-W.; Zhang, K. Y.; Li, S. P.-Y. *Pure Appl. Chem.* **2011**, *83*, 823−840.
(70) You, Y.; Nam, W. *Chem. Soc. Rev.* **2012**, *41*, 7061−7084.
(71) Duan, H.-S.; Chou, P.-T.; Hsu, C.-C.; Hung, J.-Y.; Chi, Y. *Inorg. Chem.* **2009**, *48*, 6501−6508.
(72) You, Y.; Seo, J.; Kim, S. H.; Kim, K. S.; Ahn, T. K.; Kim, D.; Park, S. Y. *Inorg. Chem.* **2008**, *47*, 1476−1487.
(73) King, K. A.; Watts, R. J. *J. Am. Chem. Soc.* **1987**, *109*, 1589−1590.
(74) You, Y.; Park, S. Y. *J. Am. Chem. Soc.* **2005**, *127*, 12438−12439.
(75) Ohsawa, Y.; Sprouse, S.; King, K. A.; DeArmond, M. K.; Hanck, K. W.; Watts, R. J. *J. Phys. Chem.* **1987**, *91*, 1047−1054.
(76) You, Y.; Kim, K. S.; Ahn, T. K.; Kim, D.; Park, S. Y. *J. Phys. Chem. C* **2007**, *111*, 4052−4060.
(77) Yeh, S.-J.; Wu, M.-F.; Chen, C.-T.; Song, Y.-H.; Chi, Y.; Ho, M.-H.; Hsu, S.-F.; Chen, C. H. *Adv. Mater.* **2005**, *17*, 285−289.
(78) Lo, K. K.-W.; Chung, C.-K.; Lee, T. K.-M.; Lui, L.-H.; Tsang, K. H.-K.; Zhu, N. *Inorg. Chem.* **2003**, *42*, 6886−6897.
(79) Li, J.; Djurovich, P. I.; Alleyne, B. D.; Tsyba, I.; Ho, N. N.; Bau, R.; Thompson, M. E. *Polyhedron* **2004**, *23*, 419−428.
(80) Dickinson, B. C.; Huynh, C.; Chang, C. J. *J. Am. Chem. Soc.* **2010**, *132*, 5906−5915.
(81) Nonoyama, M. *Bull. Chem. Soc. Jpn.* **1974**, *47*, 767−768.
(82) Tsuboyama, A.; Iwawaki, H.; Furugori, M.; Mukaide, T.; Kamatani, J.; Igawa, S.; Moriyama, T.; Miura, S.; Takiguchi, T.; Okada, S.; Hoshino, M.; Ueno, K. *J. Am. Chem. Soc.* **2003**, *125*, 12971−12979.
(83) Li, S. P.-Y.; Tang, T. S.-M.; Yiu, K. S.-M.; Lo, K. K.-W. *Chem.—Eur. J.* **2012**, *18*, 13342−13354.
(84) Lamansky, S.; Djurovich, P.; Murphy, D.; Abdel-Razzaq, F.; Lee, H.-E.; Adachi, C.; Burrows, P. E.; Forrest, S. R.; Thompson, M. E. *J. Am. Chem. Soc.* **2001**, *123*, 4304−4312.
(85) Chou, P.-T.; Liu, Y.-I.; Liu, H.-W.; Yu, W.-S. *J. Am. Chem. Soc.* **2001**, *123*, 12119−12120.
(86) Nazeeruddin, M. K.; Humphry-Baker, R.; Berner, D.; Rivier, S.; Zuppiroli, L.; Graetzel, M. *J. Am. Chem. Soc.* **2003**, *125*, 8790−8797.
(87) Chou, P.-T.; Chi, Y. *Chem.—Eur. J.* **2007**, *13*, 380−395.
(88) Hedley, G. J.; Ruseckas, A.; Samuel, I. D. W. *Chem. Phys. Lett.* **2008**, *450*, 292−296.
(89) Hedley, G. J.; Ruseckas, A.; Samuel, I. D. W. *J. Phys. Chem. A* **2010**, *114*, 8961−8968.
(90) Lo, K. K.-W.; Ng, D. C.-M.; Chung, C.-K. *Organometallics* **2001**, *20*, 4999−5001.
(91) Lo, K. K.-W.; Chung, C.-K.; Zhu, N. *Chem.—Eur. J.* **2003**, *9*, 475−483.
(92) Lo, K. K.-W.; Chung, C.-K.; Lee, T. K.-M.; Lui, L.-H.; Tsang, K. H.-K.; Zhu, N. *Inorg. Chem.* **2003**, *42*, 6886−6897.
(93) Leung, S.-K.; Kwok, K. Y.; Zhang, K. Y.; Lo, K. K.-W. *Inorg. Chem.* **2010**, *49*, 4984−4995.
(94) Miura, T.; Urano, Y.; Tanaka, K.; Nagano, T.; Ohkubo, K.; Fukuzumi, S. *J. Am. Chem. Soc.* **2003**, *125*, 8666−8671.
(95) Kennedy, D. P.; Kormos, C. M.; Burdette, S. C. *J. Am. Chem. Soc.* **2009**, *131*, 8578−8586.
(96) Rehm, D.; Weller, A. *Isr. J. Chem.* **1970**, *8*, 259−271.
(97) Suppan, P. *J. Chem. Soc., Faraday Trans. 1* **1986**, *82*, 509−511.
(98) Sajoto, T.; Djurovich, P. I.; Tamayo, A.; Yousufuddin, M.; Bau, R.; Thompson, M. E.; Holmes, R. J.; Forrest, S. R. *Inorg. Chem.* **2005**, *44*, 7992−8003.
(99) Li, X.-N.; Wu, Z.-J.; Si, Z.-J.; Zhang, H.-J.; Zhou, L.; Liu, X.-J. *Inorg. Chem.* **2009**, *48*, 7740−7749.
(100) Okamoto, K.; Fukuzumi, S. *J. Am. Chem. Soc.* **2004**, *126*, 13922−13923.
(101) Marcus, R. A. *Annu. Rev. Phys. Chem.* **1964**, *15*, 155−196.
(102) Marcus, R. A. *Angew. Chem., Int. Ed.* **1993**, *32*, 1111−1121.
(103) Kojima, T.; Hanabusa, K.; Ohkubo, K.; Shiro, M.; Fukuzumi, S. *Chem.—Eur. J.* **2010**, *16*, 3646−3655.
(104) Rosspeintner, A.; Koch, M.; Angulo, G.; Vauthey, E. *J. Am. Chem. Soc.* **2012**, *134*, 11396−11399.
(105) Dennis, A. E.; Smith, R. C. *Chem. Commun.* **2007**, 4641−4643.
(106) Tamayo, A. B.; Alleyne, B. D.; Djurovich, P. I.; Lamansky, S.; Tsyba, I.; Ho, N. N.; Bau, R.; Thompson, M. E. *J. Am. Chem. Soc.* **2003**, *125*, 7377−7387.
(107) Frisch, M. J.; Trucks, G. W.; Schlegel, H. B.; Scuseria, G. E.; Robb, M. A.; Cheeseman, J. R.; Scalmani, G.; Barone, V.; Mennucci, B.; Petersson, G. A.; Nakatsuji, H.; Caricato, M.; Li, X.; Hratchian, H. P.; Izmaylov, A. F.; Bloino, J.; Zheng, G.; Sonnenberg, J. L.; Hada, M.; Ehara, M.; Toyota, K.; Fukuda, R.; Hasegawa, J.; Ishida, M.; Nakajima, T.; Honda, Y.; Kitao, O.; Nakai, H.; Vreven, T.; Montgomery, J., J. A.; Peralta, J. E.; Ogliaro, F.; Bearpark, M.; Heyd, J. J.; Brothers, E.; Kudin, K. N.; Staroverov, V. N.; Kobayashi, R.; Normand, J.; Raghavachari, K.; Rendell, A.; Burant, J. C.; Iyengar, S. S.; Tomasi, J.; Cossi, M.; Rega, N.; Millam, N. J.; Klene, M.; Knox, J. E.; Cross, J. B.; Bakken, V.; Adamo, C.; Jaramillo, J.; Gomperts, R.; Stratmann, R. E.; Yazyev, O.; Austin, A. J.; Cammi, R.; Pomelli, C.; Ochterski, J. W.; Martin, R. L.; Morokuma, K.; Zakrzewski, V. G.; Voth, G. A.; Salvador, P.; Dannenberg, J. J.; Dapprich, S.; Daniels, A. D.; Farkas, Ö.; Foresman, J. B.; Ortiz, J. V.; Cioslowski, J.; Fox, D. J. *Gaussian 09*, Revision A.02; Gaussian, Inc.: Wallingford, CT, 2009.
(108) Becke, A. D. *J. Phys. Chem.* **1988**, *88*, 2547−2553.
(109) Becke, A. D. *J. Phys. Chem.* **1993**, *98*, 5648−5652.
(110) Becke, A. D. *Phys. Rev. A* **1988**, *38*, 3098−3100.